ISSN 1063-780X, Plasma Physics Reports, 2014, Vol. 40, No. 11, pp. 855–892. © Pleiades Publishing, Ltd., 2014.
Original Russian Text © V.A. Slemzin, F.F. Goryaev, S.V. Kuzin, 2014, published in Fizika Plazmy, 2014, Vol. 40, No. 11, pp. 967–1006.

SPACE PLASMA

Spectroscopic Diagnostics of the Solar Coronal Plasma

V. A. Slemzin, F. F. Goryaev, and S. V. Kuzin

Lebedev Physical Institute, Russian Academy of Sciences, Leninskii pr. 53, Moscow, 119991 Russia
e-mail: slem@sci.lebedev.ru

Received January 21, 2014; in final form, April 8, 2014

Abstract—The review is addressed to problems of spectroscopic diagnostics of the solar coronal plasma by its radiation in the X-ray and extreme ultraviolet (EUV) bands. Physical conditions in the corona, elementary processes and mechanisms of radiation formation, and methods and results of the temperature and density diagnostics of diverse coronal structures (such as active and quiet solar regions, coronal holes, and the extended corona) are considered. The types and main parameters of instruments for investigation of the corona by its X-ray and EUV emission in space experiments are given.

DOI: 10.1134/S1063780X14110051

1. INTRODUCTION

The physics of the solar corona is one of the fundamental directions in the solar physics research. It has been actively developed since the second half of the 20th century due to progress in space studies of the Sun and the development of relevant theoretical studies. Along with their scientific significance, studies of the processes occurring in the solar corona are also of great practical importance, because active coronal phenomena (such as flares and coronal mass ejections (CMEs)) and the solar wind flowing out of the corona are the main sources of perturbations in the heliosphere and the Earth's magnetosphere (the space environmental conditions are generally called "space weather"). The solar corona plasma is fairly hot $T \geq 10^6$ K (10^6 K = 1 MK); therefore, its radiation in the X-ray and extreme ultraviolet (EUV) spectral regions is the main source of information on the coronal conditions and phenomena, while spectroscopic diagnostics of the coronal plasma in these spectral ranges is the main method for studying the corona. Since short-wavelength solar radiation is completely absorbed by the Earth's atmosphere and does not reach the Earth's surface, such studies can be performed only in space by using instruments installed at orbital satellites, interplanetary spacecraft, or ballistic rockets reaching altitudes of higher than 100 km.

Studies of high-temperature plasma by the methods of spectroscopic diagnostics have been actively developed due to the necessity of solving important applied problems, such as controlled thermonuclear fusion, creation of X-ray lasers, and investigation of the processes occurring on the Sun and in the atmospheres of other astrophysical objects. Space experiments allowed one to record radiation of space sources in the X-ray and UV spectral bands, which provide most information on the processes occurring in the hottest plasma regions. In studies of hot laboratory plasmas, spectroscopic methods are often more preferable than contact diagnostics, because they do not perturb the object under observation, whereas information provided by the linear spectra is rather comprehensive. Thus, spectroscopic methods of plasma studies are the most universal in a rather wide range of plasma parameters and, in some cases (e.g., as applied to astrophysical objects), they are the unique source of information on the structure and dynamics of plasma.

The aim of the present paper is to give a brief review of the state of the art in the spectroscopy of X-ray and EUV radiation of the solar corona and its applications to the diagnostics of hot coronal plasma. In this review, we consider the parameters of the coronal plasma, mechanisms for the formation of X-ray and EUV radiation, and experimental and theoretical methods of hot plasma diagnostics, as well as results of studies of various coronal structures and processes that reflect progress in the physics of the solar corona and can be of interest as applied to laboratory plasma diagnostics. Recently, several monographs dedicated to the physics of the solar corona and reflecting the modern concepts on the structure of the corona and processes occurring in it (to a great extent, on the basis of the results of space studies of the Sun performed over the past 20 years) were published (see, e.g., [1–3]). In the present review, special attention is paid to the results obtained in space experiments performed in the frameworks of Russian programs (in particular, the *CORONAS* program), which have been insufficiently covered in the scientific literature.

2. GENERAL DESCRIPTION OF THE SOLAR CORONA AND CONDITIONS OF RADIATION FORMATION

The solar corona consists of inhomogeneous low-density hot plasma. Spectroscopic studies of X-ray and

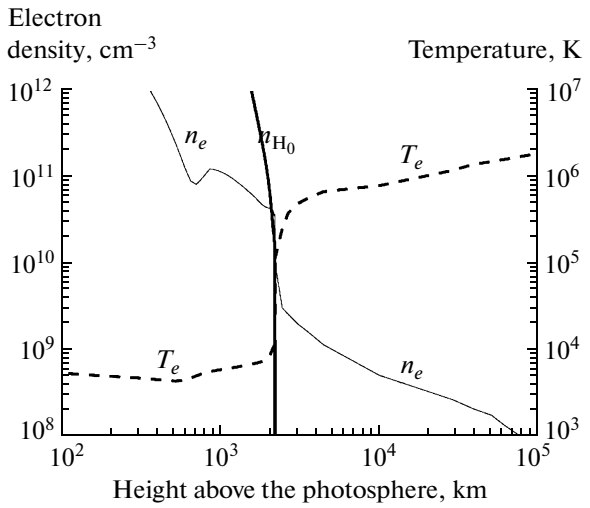

Fig. 1. Distributions of the electron density (solid curve) and temperature (dashed curve) in the model of the solar atmosphere [4, 5].

EUV emission from such plasma are aimed at the following two interrelated problems: (i) investigation of the mechanisms for the formation of radiation spectra and (ii) determination of the physical parameters of the radiation source, i.e., plasma diagnostics.

It should be emphasized that the reliability of spectroscopic methods of plasma diagnostics and even the possibility of their application depend on (i) the completeness of taking into account the elementary processes responsible for the formation of spectral lines in the plasma emission spectrum under study, (ii) the accuracy of calculating the atomic data, and (iii) the radiative plasma models based on the equations of atomic kinetics and plasma dynamics.

2.1. Parameters of the Solar Coronal Plasma and Its Radiation

The solar corona is the outer shell of the solar atmosphere passing over to the heliosphere. The lower part of the solar atmosphere consists of the photosphere (conditionally located at heights from 0 to 320 km), the chromosphere (from 320 to 2000–3000 km), and the transition region of thickness 70–100 km between the chromosphere and the corona. Here, the height is counted from the lower boundary of the photosphere, below which solar plasma becomes optically thick for its visible self-radiation (λ = 5000 Å). The distributions of the electron density and temperature in the plane-parallel model of the solar atmosphere obtained by solving the equations of radiative transfer in the hydrostatic equilibrium approximation [4, 5] are shown in Fig. 1. According to the model of the average atmosphere [6], the plasma temperature in the photosphere is about 6400 K. In the chromosphere, it first decreases to 4400 K at a height of about 500 km and then gradually increases again to 10^4 K. In the transition region, the temperature increases stepwise from 10^4 to $(2–3) \times 10^5$ K; then, in the lower corona, it increases to the coronal value of $(1–2) \times 10^6$ K.

The main source of information on the processes occurring on the Sun is its radiation in different wavelength ranges associated with solar regions characterized by certain values of the temperature, plasma density, and the magnetic field strength. Since the brightness of visible radiation of the solar corona near the limb is on the average six orders of magnitude lower than that of the solar disk, observations of the corona are hampered by the scattered light of the solar disk. The visible corona is usually observed using ground- and space-based coronagraphs starting from a certain distance from the limb (from several tenths of the solar radius to one solar radius). The entire visible corona can be observed only during solar eclipses (Fig. 2a).

Usually three components are distinguished in the visible corona radiation: (i) the polarized K-corona, which has a continuous spectrum and forms due to the Thomson scattering of photospheric visible radiation from free electrons; (ii) the unpolarized F-corona, which has a Fraunhofer spectrum and forms due to the scattering of photospheric radiation from interplanetary dust; and (iii) the emission L-corona (or E-corona), which consists of the lines of highly charged Fe X–XIII, Fe XVII, C VI, O VI–VIII, Mg X–XII, Si XI, and other ions excited at temperatures of 1–2 MK. The K- and E-components are observed in the inner corona (up to $3R_\odot$, where $R_\odot$ is the solar radius). At larger distances, the F-component gradually transforming into the zodiacal light dominates. Using space-based coronagraphs, the corona is usually observed up to distances on the order of $30R_\odot$; however, when the denser CMEs propagate in the corona, they can be traced using wide-angle cameras up to the Earth's orbit ($\sim 200R_\odot$).

The solar coronal plasma is characterized by the high temperature, which is 1–2 MK in the quiet state and reaches 20–100 MK in powerful flares. At such high temperatures, the macroscopic stability of the coronal plasma is provided by the balance between its thermal pressure and the magnetic field pressure. The solar magnetic field produced by sources located below the photosphere can be conditionally divided into two components: (i) the strong local field closed on the Sun's surface and (ii) the weak global field penetrating into the heliosphere in the form of open field lines. During the most part of the solar cycle, the global magnetic field has a dipole structure and changes its sign in the maximum of solar activity. Since direct measurements of the magnetic field in the corona are impossible, its structure and strength are calculated using various models. The global solar magnetic field is calculated by means of the potential field model. As boundary conditions, the model employs the photo-

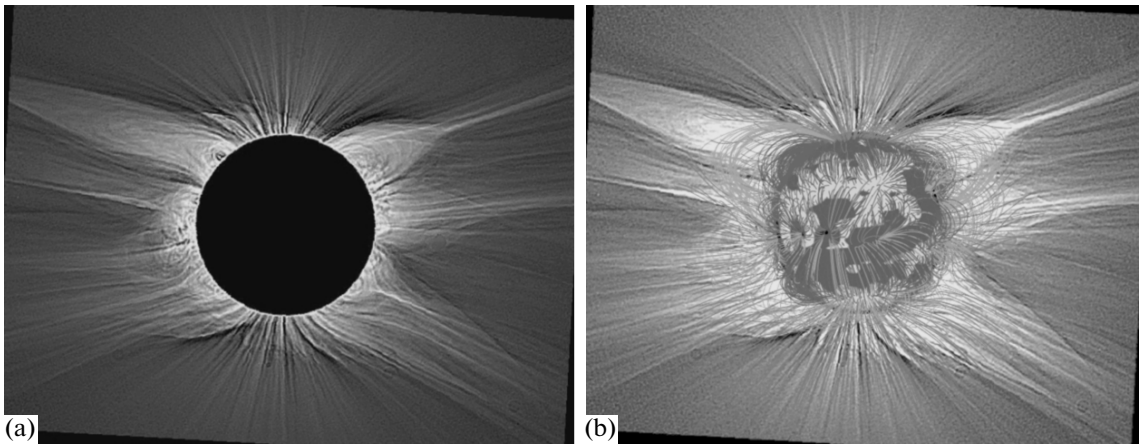

Fig. 2. (a) Solar corona in visible light during the total eclipse on March 29, 2006 [7] and (b) coronal magnetic field structure calculated using the potential field model.

spheric magnetic field maps constructed using the data obtained with ground-based magnetographs. The field lines above the conditional source surface situated at a distance of $2.5R_\odot$ are assumed to be strictly radial (Fig. 2b).

The strongest magnetic fields (up to 1000–3000 G) are generated in the closed loops of large active regions (ARs), which, as a rule, are associated with sunspots. In the quiet regions (QRs), the magnetic field is much weaker (10–30 G) and is concentrated in multiple low loops forming the so-called "magnetic carpet." There are also extended regions with an open magnetic field on the Sun—the so-called "coronal holes" (CHs) with an average magnetic field on the order of 100 G. At the solar minimum, the largest CHs are situated in the polar regions. As the maximum of the activity is approached, the polar CHs decrease in size and are gradually displaced toward the equator. When they reach the equator at the solar maximum, the polarity of the global magnetic field reverses. At high solar activity, besides the polar CHs, some low-latitude CHs that can exist for several solar rotations appear near the equator.

The most significant appearances of solar activity are observed in the solar corona in the temperature range from a few hundred thousands to several tens of millions of kelvins and are recorded in the soft X-ray (SXR) (1–100 Å) and EUV (100–2000 Å) wavelength bands. Since the photosphere does not radiate in these spectral regions, the images taken in different spectral channels show the structure of the corona in the corresponding temperature ranges (Fig. 3).

The bursts of solar activity caused by a pulsed release of enormous energy (10^{25}–10^{26} J) are accompanied by a sharp increase in the radiation flux (flares), CMEs, and ejections of high-energy charged particles into the heliosphere. Studies of the dynamics of these processes and the accompanying phenomena in the chromosphere and corona are important for determining the physical nature of solar activity; constructing theoretical models; and, eventually, predicting the probable geophysical consequences (see, e.g., [8]).

The structure and local parameters of the solar corona are closely related to the structure and strength of the magnetic field. ARs with closed magnetic loops and the strongest magnetic field contain hot dense plasma; therefore, they have the highest brightness in the X-ray and EUV ranges. In contrast, the magnetic

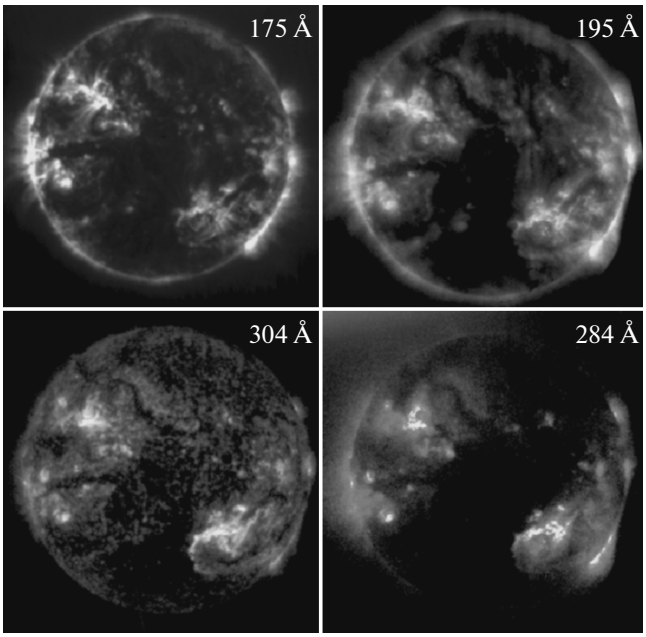

Fig. 3. EUV images of the Sun obtained on December 11, 2001, in the 175-, 195-, 284-, and 304-Å channels of the *SPIRIT* telescope, corresponding to the excitation temperatures of 1, 1.6, 2, and 0.05 MK, respectively.

Table 1. Typical parameters of solar corona structures observed in the EUV and X-ray spectral bands

Structure type	Characteristic size	Lifetime	Temperature	Density, cm^{-3}
Active regions	3′–5′	Up to 1–2 rotations	1–3 MK	10^9
Coronal holes	1′–10′	Up to 5–6 rotations	1 MK	10^8
Quiet regions	Entire disk	Permanently	1–1.5 MK	5×10^8
Filaments, prominences	10″–10′	Up to 2–3 rotations	6000 K in the core, up to 1 MK in the shell	10^{11}–10^{12} (core)
Streamers	Up to (2–3)$R_\odot$ in length, (0.1–0.5)$R_\odot$ in thickness	Up to 1–2 rotations	1.4–1.7 MK	10^8 (limb)–10^6 ($2R_\odot$)
Flare regions	≥1″	10 min–3 h	2–100 MK	10^9–10^{10}
Coronal mass ejections	0.1–5$R_\odot$	0.5–2 h (motion in the field of view)	0.1–2 MK	10^5–10^6 (at a height of ~1$R_\odot$ above the limb)

field in CHs is low and consists of open field lines; therefore, they are colder and the plasma density in them is lower by one order of magnitude. As a result, the brightness of these regions of the solar disk is lower than that of ARs and QRs. The QRs occupy most of the solar disk, and the plasma density in them is intermediate between that in CHs and ARs. At distances of several solar radii, the global magnetic field in the corona is formed of open magnetic field lines and plasma is concentrated in the ray-like streamer structures observed near the solar surface in the EUV spectral region. At larger distances, these structures can be observed in the scattered visible light. Drastic changes of the structure of the coronal magnetic field occur during active phenomena (flares and CMEs), because, in these events, as a result of magnetic reconnection, the accumulated magnetic energy is converted in the explosive manner into the energy of charged particle beams, light energy, and the kinetic energy of the ejected plasma.

Besides large-scale structures (CHs, ARs, and QRs), there are also medium- and small-scale coronal structures observed in the X-ray and EUV spectral regions, such as absorbing filaments seen on the disk and radiating prominences seen at the limb, as well as small-scale transient structures with lifetimes from several minutes to a few hours, such as polar plumes, jets, sprays, surges, macrospicules, etc. Jets, sprays, and surges are narrow diverging plasma ejections formed from cold dense gas streams ejected from the chromosphere and heated by small flares in their bases. They are observed at the polar limb and near the ARs in the X-ray and EUV spectral regions. The polar plumes are ray-like structures stretching along open magnetic field lines of the polar CHs and observed at the limb in the visible and EUV spectral regions. The parameters of the main structures of the solar corona are given in Table 1.

Stability of the coronal plasma structures formed by the magnetic field depends on the ratio β of the plasma thermal pressure to the magnetic field pressure [1],

$$\beta = \frac{p_{th}}{p_{mf}} = \frac{2\xi n_e k_B T_e}{B^2/8\pi}, \quad (2.1)$$

where ξ is the degree of ionization of the coronal plasma, k_B is the Boltzmann constant, B is the magnetic field strength, n_e is the electron density, and T_e is the electron temperature. The distribution of the parameter β in the solar atmosphere is shown in Fig. 4 [9].

In the most of the corona, $\beta < 1$; therefore, plasma is confined by the magnetic field. However, in the high-density plasma at the corona–chromosphere boundary and in hot structures observed at heights above 200000–300000 km (~0.3–0.5 of the solar radius), the plasma pressure can exceed the magnetic pressure, which leads to the smearing of coronal structures due to the escape of plasma across magnetic field lines and the formation of local solar wind flows.

X-ray and EUV spectra of the corona are the main source of information on the state of coronal plasma and the processes occurring in it. The brightest resonance lines of ions of the most abundant elements (such as C, O, Mg, Si, and Fe) excited at temperatures of 0.1 to 100 MK lie just in these spectral ranges. The most often used in the diagnostics of the coronal plasma are the lines of Fe VII–Fe XXIV ions (Fig. 5). These lines lie close to one another in the EUV spectral region, are emitted by almost all coronal structures, and cover the most important temperature range of $\log_{10}(T\,[\mathrm{K}]) = 5.4$–$7.0$ (Fig. 5).

In a wide range of plasma densities (from 10^9 cm^{-3} in the limb to 10^6 cm^{-3} at a distance on the order of two solar radii), the coronal plasma is in the state of local coronal equilibrium. The coronal equilibrium model is applicable to low-density optically thin plasma in which the charge state of an ion and the populations of ion energy levels are determined by the balance

between electron collisions and radiative decay. In this case, the intensities of spectral lines measured with high spatial and temporal resolutions provide information on the parameters and spatial structure of the coronal plasma, the processes of the plasma heating and cooling, plasma kinetics, macroscopic plasma motion, etc. The coronal plasma is usually optically thin, except for the near-limb regions, ARs, flare regions, filaments, and prominences, where the optical thickness can be on the order of or larger than unity because of the high plasma density (higher than 10^{10} cm^{-3}) or significant integration paths for some strong spectral lines. The main mechanism of the generation of X-ray and EUV line radiation in the corona are electron collisions; however, in the low-density outer corona, radiative excitation (in particular, resonance scattering) can prevail over collisional excitation [10–14].

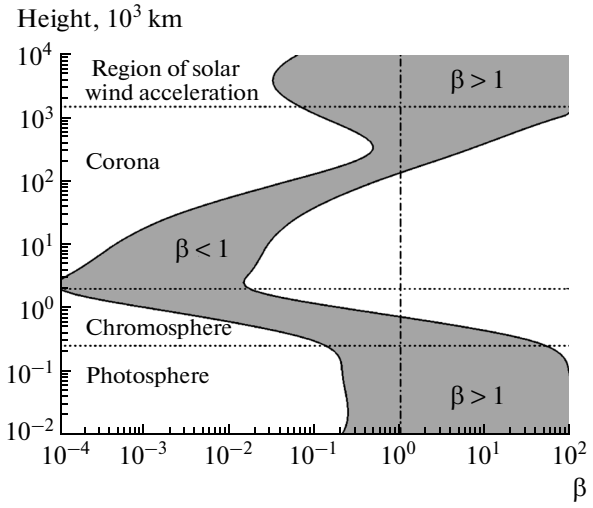

Fig. 4. Distribution of the β parameter over the height in the solar atmosphere [9].

2.2. Element Abundances in the Solar Photosphere and Corona. FIP Effect

The line intensities of different elements in the emission spectrum of the corona are proportional to the concentrations of these elements usually characterized by their abundances with respect to hydrogen. The element abundance is defined as follows:

$$A_{\mathrm{el}} = \log\left(N_{\mathrm{el}}/N_{\mathrm{H}}\right) + 12.0,$$

where $N_{\mathrm{el}}/N_{\mathrm{H}}$ is the ratio between the concentrations of the given element and hydrogen.

The element abundances in the photosphere are determined from the Fraunhofer absorption lines of neutral atoms or singly charged ions observed on the Earth in the visible spectral region. The element abundances in the solar photosphere almost coincide with the elemental composition of the meteoritic matter [15, 16], which indicates that all objects in the solar system were formed from the same primary material.

When passing from the chromosphere to the corona, the absorption spectrum becomes emissive due to the increase in the temperature from a few hundred thousands to several million kelvins. The radiation is emitted by highly charged ions and shifted into the EUV range. Analysis of the coronal radiation spectra recorded on satellites shows that the coronal abundances of all elements are divided into two groups [16, 17]. The abundances of elements with the first ionization potentials (FIPs) (i.e., the potentials of ionization from the neutral state into a singly charged ion) of higher than 10 eV (such as H, O, C, and N) are the same as in the photosphere. The abundances of elements with FIPs lower than 10 eV (such as Si, Mg, Fe, Ca, Al, K, and Na) in the corona are much higher than those in the photosphere (the FIP effect). The ratio between the concentrations of an element in the corona and the photosphere is called the FIP bias. For elements with low FIPs, it is, on the average, 4. Table 2 gives standard abundances and FIP biases for 15 most abundant elements in the photosphere and QRs of the corona [17].

According to theoretical models (see, e.g., [18]), a jump in the element abundances when passing from the photosphere to the corona is caused by the two processes: photoionization of low-FIP atoms in the chromosphere by the Lyα hydrogen radiation at a temperature below 10^4 K and the subsequent separation of ions and high-FIP neutrals due to the difference in their diffusion rates. Estimates show that the thickness of the solar atmospheric layer in which ionization and separation occur is only a few kilometers; hence, ions have time to leave it before they recombine. Within each group of elements, the ratios of the abundances are nearly equal to their photospheric values; i.e., the atomic mass of an element within such short distances plays a minor role (gravitational separation of elements with different atomic masses that is not associated with the FIP effect manifests itself at larger heights in the extended corona [16]).

In practice, the relative abundances of elements with low and high ionization potentials (such as Mg/O, Fe/O, and Si/O), which are determined from the relative intensities of close pairs of lines of these elements, are often used to characterize the FIP bias.

The element abundances and the FIP bias for individual coronal structures can differ substantially from their standard values for the quiet corona [17]. The bias value in the ARs depends on the "age" of their magnetic loops. In nascent loops, the abundances are close to their photospheric values; however, two to three days later, the bias reaches its coronal value of 4 and, after one to two weeks, increases to 7–14. In the flares, the bias varies from 1 to 4, because they most often occur in young developing ARs. In contrast, in the CHs, the abundances almost coincide with their

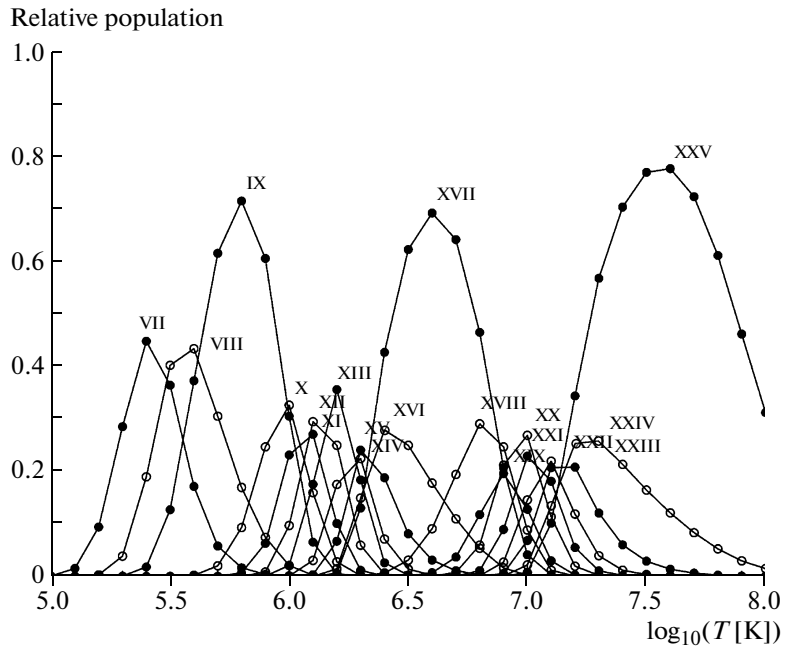

Fig. 5. Relative populations of Fe ions in different ionization states (calculated by means of the CHIANTI code) as functions of the temperature.

photospheric values, provided that there are no emerging ARs in them.

The fact that the element abundances depend on the type of coronal structures is very important for the identification of sources of the solar wind, the ion composition of which depends on the wind velocity [17, 19]. In the high-speed wind with a velocity of $v >$ 600 km/s, the relative abundances of elements correspond to their photospheric values, which suggests that the sources of such a wind can be identified as CHs. The ion composition of the low-speed wind ($v <$ 500 km/s) corresponds to FIP biases from 1 to 4, which indicates that it originates from the plasma of ARs; in this case, the specific mechanism of the wind outflow can be different.

2.3. Elementary Processes in the Solar Plasma and Mechanisms of the Generation of X-ray and EUV Emission

In high-temperature plasma, X-ray and EUV emission is mainly generated due to electron–ion collisions. The bremsstrahlung and recombination continuums, as well as line radiation caused by the transitions between ion energy levels, are generated due to electron scattering by nuclei of light elements (protons and α-particles) and highly charged ions. The emission spectra contain information on both their emitters and the state of the ambient plasma. The shape of the spectrum depends on many factors: the energy structure of elementary emitters (highly charged ions), the character of electron–ion collision interaction (resulting in the excitation, ionization, recombination, and other processes), and the plasma state as a whole (steady-state or transient (nonequilibrium)). The continuum mainly contains information on the electron component (the spatial and energy distributions of electrons), while the line radiation is also determined by the specific features of the heavy component (the structure of electron shells of ions and the character of electron–ion collision interaction).

The main elementary electron–ion interaction processes in the solar corona are inelastic collisions and dielectronic recombination. Most lines with a wavelength shorter than 2000 Å are formed due to inelastic collisions. Dielectronic recombination leads to the excitation of levels lying above the ionization potential and the formation of dielectronic satellites—spectral lines emitted by highly charged ions in the X-ray spectral region. The other processes, such as proton–ion collisions, photoexcitation, resonance scattering, ionization, and recombination, also contribute to the radiation; however, their contribution is usually less significant than that of electron–ion collisions.

It should be noted that, till now, the roles played by different mechanisms in the formation of EUV radiation of the extended solar corona have been studied insufficiently well due to the lack of the data on the plasma parameters at such large distances from the Sun's surface. For example, it was asserted in [20] that the collisional mechanism was the unique process contributing to the formation of EUV radiation detected by the 174 Å channel of the PROBA2/SWAP telescope, which records radiation of Fe IX–Fe XI

ions. Since the solar disk practically does not radiate in the wavelength range below 1000 Å, the authors of [20] assumed that resonance scattering in these spectral lines could be ignored. However, in the upper corona, these ions can absorb and reemit photons generated by similar ions in the lower corona, where the plasma density is much higher and the radiation flux can be significant. Such a resonance scattering process is more efficient than radiative excitation by the continuum arriving from the colder photosphere. It should be also noted that this process depends substantially on the correlation between the spectral profiles of the incident and scattered radiation. In particular, when the solar plasma moves along the radius, the contribution of resonance scattering decreases due to the Doppler shift (the Doppler dimming effect).

The collisional excitation rate is proportional to the product of the ion and electron densities (i.e., to the square of the electron density), whereas the rate of resonance scattering is proportional only to the ion density. As a result, at sufficiently large distances from the Sun's surface, where the plasma density decreases by one to two orders of magnitude, the collisional excitation rate decreases by two to four orders of magnitude, due to which the contribution of resonance scattering to EUV radiation can become comparable with that of collisional excitation and even dominant. Even near the limb, where the plasma density is high, the contribution of resonance scattering to the corona radiation along the line of sight can lead to an increase in the plasma optical thickness, which in turn affects the intensities and profiles of X-ray and EUV spectral lines. This effect can also be used for the spectroscopic diagnostics of the plasma parameters. Estimates of the contributions of the collisional and resonance mechanisms of emission excitation in the extended corona depend on the radial distributions of the electron density, temperature, and plasma flow velocity in the coronal structures. These parameters can be determined by the methods of spectroscopic diagnostics with the use of observational data.

2.4. X-ray and EUV Spectra

Let us consider the main relationships governing the X-ray and EUV spectra of plasma under the coronal conditions. The total power per unit volume emitted in a spectral line corresponding to the transition $i \to k$ is characterized by the total emissivity function $\varepsilon_{ik}(\mathbf{r})$ (in units of photon cm^{-3} s^{-1}),

$$\varepsilon_{ik} = N_i A_{ik}, \tag{2.2}$$

where N_i (in cm^{-3}) is the population density for the upper (i) level of the emitting ion and A_{ik} (in s^{-1}) is the spontaneous probability for the radiative transition $i \to k$. The population densities N_i of atoms and ions in plasma are determined by solving the following system of kinetic equations of balance:

$$\frac{dN_i}{dt} = \sum_{m \neq i} N_m W_{mi} - N_i \sum_{n \neq i} W_{in}, \tag{2.3}$$

where W_{mn} (in s^{-1}) is the total probability rate coefficient for the transition $m \to n$ due to radiative and collisional processes and the integer indices n, m, i, etc., are used to enumerate the energy states of an ion characterized by the charge z and the set of quantum numbers α.

System (2.3) can be solved numerically in the framework of the adopted atomic collisional-radiative model in which the most important elementary processes determining the distribution of the ion level populations are singled out for each particular case. Due to the functional dependences of the rate coefficients W_{mn}, the populations N_i are functions of the electron temperature T_e and electron density N_e, as well as of the parameters of the velocity distribution functions of plasma particles. When the left-hand side of Eq. (2.3) is zero, plasma is in a steady or quasi-steady state. In the general case, terms related to the plasma motion, diffusion, and other processes and leading to the spatiotemporal nonequilibrium of ion populations should be added to the left-hand side of Eq. (2.3).

Table 2. Standard element abundances in the solar photosphere and quiet solar corona [15]

Atomic number	Element	Ionization potential, eV	Photospheric abundances	Coronal abundances	FIP bias
1	H	13.6	12.00	12.00	1
2	He	24.6	10.93	10.93	1
6	C	11.3	8.52	8.52	1
7	N	14.5	7.92	7.92	1
8	O	13.6	8.83	8.83	1
10	Ne	21.6	8.11	8.11	1
11	Na	5.1	6.32	6.92	4
12	Mg	7.6	7.58	8.18	4
13	Al	6.0	6.49	7.09	4
14	Si	8.2	7.56	8.16	4
16	S	10.4	7.33	7.33	1
18	Ar	15.8	6.59	6.59	1
20	Ca	6.1	6.35	6.95	4
26	Fe	7.9	7.50	8.10	4
28	Ni	7.6	6.25	6.85	4

The observed total line intensity I_{ik} (in units of photon cm^{-2} s^{-1}) of an optically thin plasma source corresponding to the transition $i \to k$ is determined by the volume integral

$$I_{ik} = \frac{1}{4\pi R^2}\int_V \varepsilon_{ik}(\mathbf{r})dV, \quad (2.4)$$

where integration is performed over the entire emitting volume V and R is the distance from elementary emitter to the observation point.

The interaction between plasma particles leads to the broadening of ion spectral lines. The widths of the lines emitted by an optically thin hot plasma is mainly determined by the Doppler effect (the broadening caused by thermal motion of the emitting ions), as well as by the natural line width (the Lorentz broadening) characterized by the lifetime of the upper level (i.e., the total probability of decay) for a given transition. In order to take into account the broadening of the ion spectral lines in plasma, the spectral density of the volume emissivity is introduced,

$$\varepsilon_l(\lambda) = \varepsilon_{ik}\varphi(\lambda - \lambda_l), \quad (2.5)$$

where $\varphi(\lambda - \lambda_l)$ is the line profile normalized to unity and λ_l is the central wavelength of the spectral density. Introducing the spectral intensity in the line l corresponding to the transition $i \to k$,

$$I(\lambda - \lambda_l) = \frac{1}{4\pi R^2}\int_V \varepsilon_{ik}(\mathbf{r})\varphi(\lambda - \lambda_l)dV, \quad (2.6)$$

and the spectral distribution $I^{(C)}(\lambda)$ of the continuous spectrum of plasma radiation, we obtain the whole spectrum,

$$I(\lambda) = \sum_i I(\lambda - \lambda_i) + I^{(C)}(\lambda) = \frac{1}{4\pi R^2}\int_V \tilde{F}(\lambda, \mathbf{r})dV, \quad (2.7)$$

where the total spectral density $\tilde{F}$, including the continuous component $F^{(C)}$, has the form

$$\tilde{F}(\lambda, \mathbf{r}) = \sum_l \varepsilon_l(\mathbf{r})\varphi(\lambda - \lambda_l) + F^{(C)}(\lambda, \mathbf{r}). \quad (2.8)$$

As an example, Figs. 6 and 7 show the EUV radiation spectra of a QR and an AR of the Sun in the spectral ranges of 170–210 Å (Fig. 6) and 240–330 Å (Fig. 7). These are the spectral ranges that were recorded in the *CORONAS/SPIRIT* experiment and in which the *Hinode/EIS* spectrograph operates since 2007. The calculations were performed using the CHIANTI software package (see Section 2.6) with the corresponding model distributions of the plasma parameters in the QR and AR.

2.5. Conditions of Thermodynamic Equilibrium

Because of the complexity of the processes of plasma particle interaction, the description of the plasma state is a rather difficult problem, which can be solved only in some limiting cases. To study nonequilibrium plasma in a general case, it is necessary to have information on the elementary interaction processes and their cross sections, as well as on the atomic characteristics.

At sufficiently high plasma densities and large dimensions of the region occupied by the plasma, conditions of the total thermodynamic equilibrium (TE) are implemented. Under these conditions, the physical state of plasma is completely determined by the finite number of thermodynamic parameters. As a rule, laboratory and astrophysical plasmas are never in the total TE state. However, the relationships characterizing the TE are often useful. For example, many finite-size plasma objects can be in a state that insignificantly differs from the total TE (the so-called local thermodynamic equilibrium (LTE)). Moreover, under the TE conditions, the principle of detailed balance in which direct and inverse processes for any atomic interaction proceed at the same rates (i.e., compensate for one another) is satisfied. Using this principle, it is possible to obtain the relationships between the rates of direct and inverse processes.

Under the LTE conditions, the plasma state is determined by three distribution functions: the Maxwellian electron velocity distribution, the Boltzmann distribution for the populations of atomic levels, and the ionization equilibrium distribution (the Saha distribution). These distributions are completely determined by the local values of the plasma temperature T and electron density N_e.

The Maxwellian distribution of the electron gas is rather stable, because electrons exchange their energies very intensively. This distribution can also take place when the other parameters and distributions (e.g., the Boltzmann and Saha distributions) deviate from equilibrium. In this case, the temperature T entering into the formula of the Maxwellian distribution loses its strict sense and is substituted with the so-called kinetic temperature. It often turns out that electrons, on the one hand, and heavy particles (ions or atoms), on the other hand, are described by distributions with different kinetic temperatures. In this case, plasma is in a quasi-steady state with different temperatures of electrons (T_e) and ions (T_i). The ionization equilibrium for such plasma is usually described by the parameter T_Z, which is determined as the ionization temperature corresponding to the observed ion distribution. Then, the condition $T_Z = T_e$ corresponds to plasma in a steady state, $T_Z < T_e$ corresponds to the ionizing plasma, and $T_Z > T_e$ corresponds to the recombining plasma.

In the limit of low plasma densities ($N_e \to 0$), the populations of excited atomic levels in plasma are very low (much lower than those corresponding to the Boltzmann distribution). Such a situation is typical of

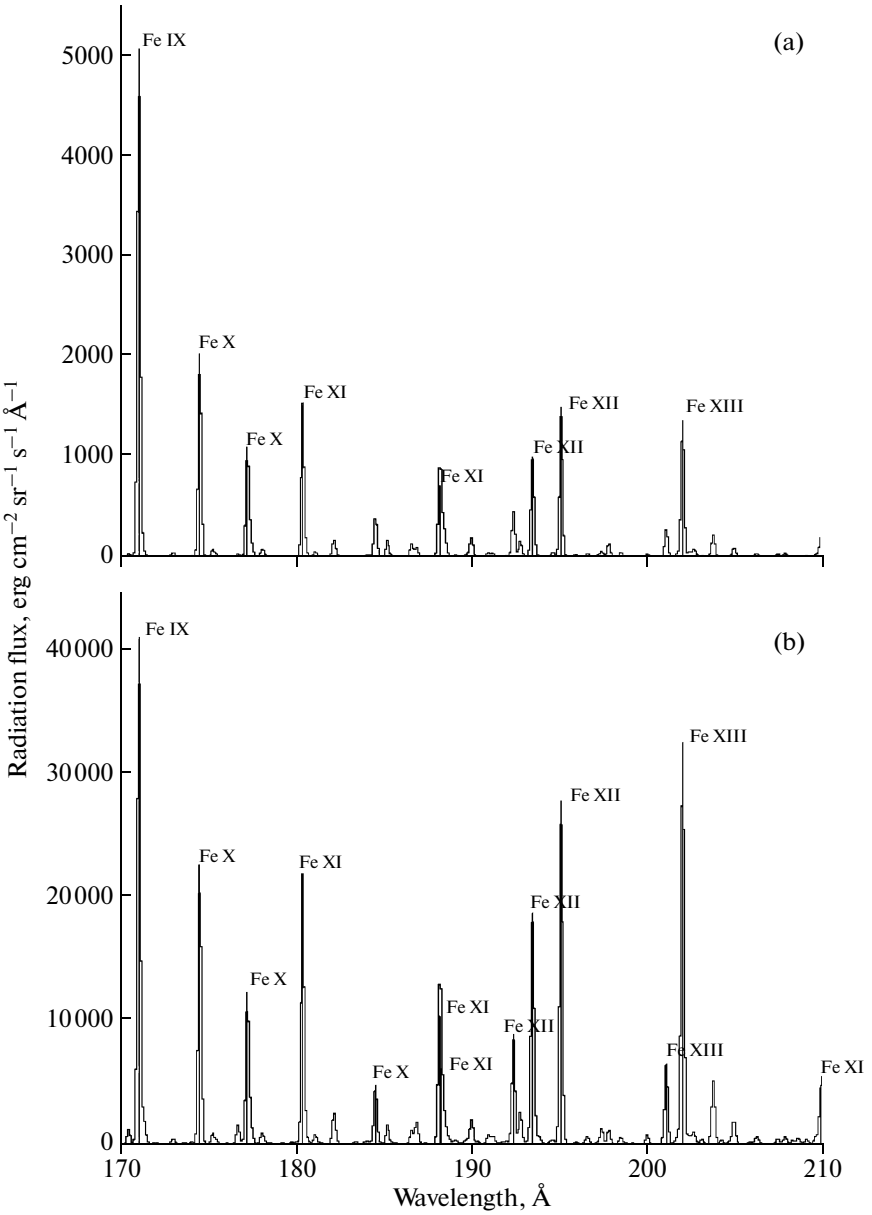

Fig. 6. EUV spectra in the 170–210 Å wavelength band for (a) the quiet Sun and (b) an active region, calculated by means of the CHIANTI code.

the solar corona plasma (the coronal approximation (CA)), in which the densities are much lower than those in laboratory plasmas. To estimate the populations of energy levels and the line intensities in the CA, it is necessary to take into account that the excitation of all levels and ionization occur only from the ground state ($k = 0$) and the only mechanism of relaxation of the ith excited state is spontaneous decay. When the branching ratio is unity (i.e., when there is only one radiative channel $i \to k$), the radiation intensity does not depend on the probability of spontaneous emission A_{ik} and is determined only by the excitation rate of the ith state. This is an important feature of the CA.

When neither of the two above limiting cases take place, the population densities of atomic levels are determined by the entire set of radiative and collisional processes taken into account in the radiative-collisional plasma model based on the system of kinetic equations of balance (2.3). In the intermediate range of plasma densities, long-lived (metastable) states undergo collisional mixing or ionization, which leads to the redistribution of the emitted energy in the line spectrum. The transition region from the CA to the Boltzmann distribution corresponds to the condition

$$N_e^* \approx A_{ik}/C_{ik}, \qquad (2.9)$$

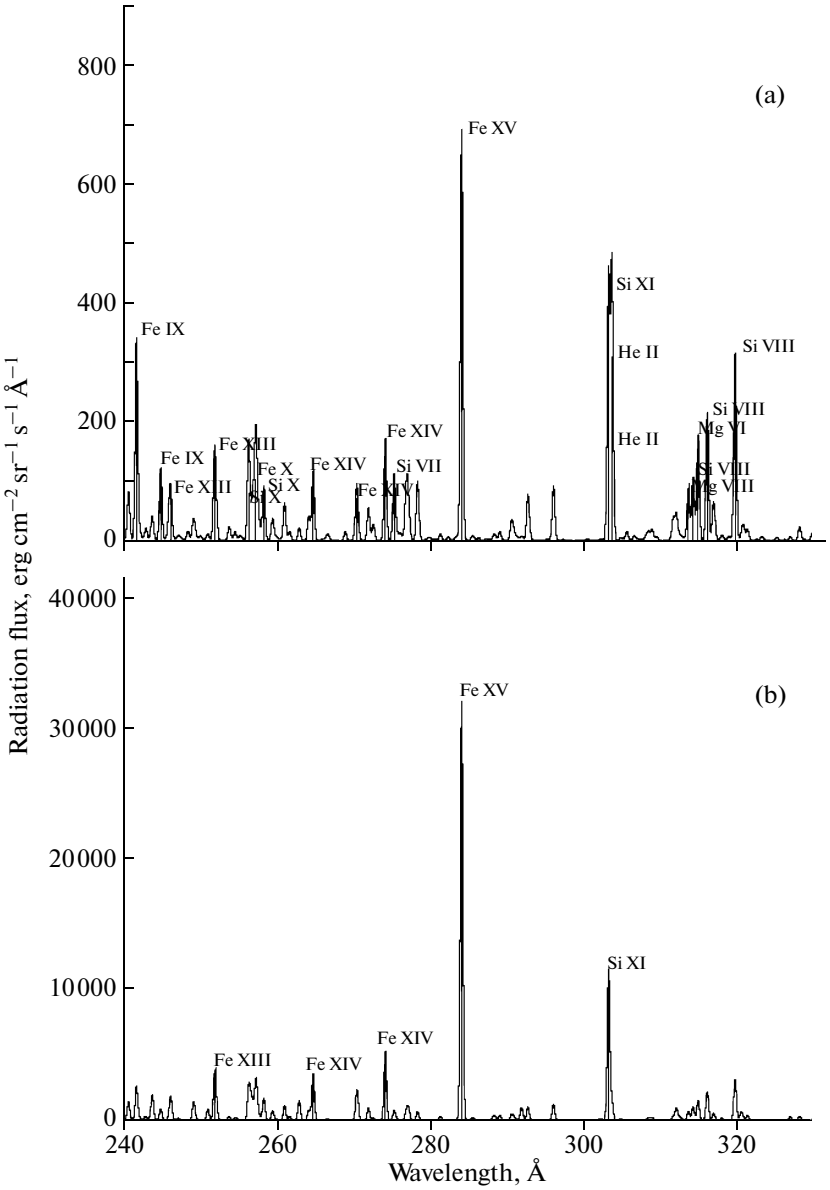

Fig. 7. EUV spectra in the 240–330 Å wavelength band for (a) the quiet Sun and (b) an active region, calculated by means of the CHIANTI code.

where N_e^* is the critical density separating regimes with different characters of the distribution of the population densities of excited levels in plasma and C_{ik} is the collisional excitation rate of the ith level from the ground state. At densities of $N_e \ll N_e^*$, which are typical of astrophysical plasmas, we have the limiting case corresponding to the CA. In the opposite case $N_e \gg N_e^*$, which usually takes place in laboratory plasmas, the population densities of excited levels satisfy the equilibrium Boltzmann distribution.

It is also worth saying some words about steady-state conditions in plasma. Such conditions mean that the characteristic relaxation times for electrons, ions, and the ionization equilibrium (τ_e, τ_i, and τ_z, respectively) are much shorter than the time τ of radiation observation. In addition, it is assumed that the distributions of electrons and ions, as well as the distribution of ion species, are independent of time. The opposite case of a non-steady-state plasma means that $\tau \ll \tau_e, \tau_i, \tau_z$. In the intermediate case of transient plasma, the conditions $\tau_e \ll \tau < \tau_i, \tau_z$ are satisfied.

2.6. Codes for Calculation of the Emission Spectra of the Coronal Plasma

At present, there is a number of software packages for calculating plasma spectra under solar coronal

conditions and analyzing the results of spectral measurements.

CHIANTI. The CHIANTI package [21] consists of a set of critically selected and computed atomic data for many ions that are of interest for astrophysical objects radiating in the X-ray and EUV spectral bands. It also includes auxiliary data and a set of Interface Definition Language (IDL) procedures for calculating the synthetic spectra of optically thin plasma sources and performing spectral analysis and plasma diagnostics. The CHIANTI database is widely used to analyze the line radiation spectra of astrophysical sources.

SPEX. The SPEX (SPectral EXecutive) package [22] provides a unified interface intended to analyze data from various X- and gamma-ray spectral instruments. Using this package, it is possible to analyze data from solar flares and bursts, as well as plot light curves of these solar events.

APEC/APED. The APEC/APED package is the Astrophysical Plasma Emission Code (APEC)—a collisional-radiative plasma code written in the C language [23]—combined with the atomic data from the Astrophysical Plasma Emission Database (APED) for calculating the line and continuum radiation from hot collisional plasmas as functions of the temperature and the ionization state.

PINTofALE. The PINTofALE (Package for the INTeractive Analysis of Line Emission) [24] package was elaborated to analyze the radiation spectra of the optically thin coronal plasma in the spectral range of 1–1500 Å. It includes a set of IDL programs combined with the atomic and observational data bases. These programs allows the user to easily identify spectral lines, measure radiation fluxes, and perform detailed simulations.

These software products can also be used to analyze spectral data from other astrophysical objects.

3. INSTRUMENTS AND METHODS FOR X-RAY AND EUV SPECTROSCOPY OF THE SOLAR CORONA

Instruments for photometry and spectroscopy of the solar corona can be divided into the following five main types:

(i) X-ray and EUV spectrophotometers,

(ii) high-resolution X-ray spectrometers and spectroheliometers,

(iii) X-ray broadband telescopes and spectrometers,

(iv) spectrally selective EUV telescopes with multilayer optics, and

(v) diffractive EUV spectrometers and spectroheliometers.

As was noted above, studies of the solar spectra in the X-ray and EUV spectral bands can be performed only at altitudes higher than 100 km because of strong absorption of these radiations in the atmosphere. Below, we will consider the main types of instruments for spectroscopic studies of the solar corona onboard spacecraft.

3.1. X-ray and EUV Spectrophotometers

The main goal of observations of the Sun by using X-ray and EUV photometers is to monitor solar radiation in several wide spectral subranges in order to determine the current level of solar activity and observe solar flares. This information is one of the most important components of monitoring space weather. These instruments are broadband radiation detecting devices the spectral sensitivity of which is determined by the properties of the detector and filter. When using detectors the amplitude of signals from which is proportional to the energy of detected photons (as is the case, e.g., in the SphinX X-ray spectrophotometer) and applying amplitude analyzers, it is possible to achieve spectral resolution sufficient to distinguish individual spectral lines.

Data from two-channel X-ray spectrophotometers installed at the geostationary satellites of the *GOES* (*Geostationary Operational Environmental Satellite* [25]) series (United States) are used for a wide range of tasks. The first satellite of this series was launched in 1975. At present, the measurements are being performed on the *GOES-13*, *GOES-14*, and *GOES-15* satellites of the third generation, launched in 2006, 2009, and 2010, respectively. The *GOES* equipment includes X-ray sensors (XRSs) of solar radiation, which are ionization chambers equipped with Be filters. The measurements are performed in the spectral ranges of 0.5–4 and 1–8 Å (Fig. 8). Real-time data on the X-ray solar radiation averaged over 1 and 5 min, as well as the corresponding time plots, can be found at the site of the Space Weather Prediction Center (SWPC) of the U. S. National Ocean and Atmosphere Administration (NOAA) (http://www.swpc.noaa.gov/Data/index.html#measurements).

The classification of solar X-ray flares is based on measurements of absolute fluxes of solar X-ray emission by using *GOES* instruments. The classification scale includes flares of five classes (A, B, C, M, and X) characterized by the following peak fluxes in the spectral range of 1–8 Å: from 10^{-8} to 10^{-7} W/m^2 for class A, from 10^{-7} to 10^{-6} W/m^2 for class B, from 10^{-6} to 10^{-5} W/m^2 for class C, from 10^{-5} to 10^{-4} W/m^2 for class M, and higher than 10^{-4} W/m^2 for class X. The flares with fluxes below 10^{-8} W/m^2 lie below the sensitivity threshold of the detector, and those with fluxes above 10^{-3} W/m^2 lead to the nonlinearity and saturation of the detector. The strongest flare of class X28 with a flux of 2.8×10^{-3} W/m^2 was detected on November 4, 2003. The *GOES* data are used to estimate the temperature of the flare plasma from the ratio of the X-ray fluxes in

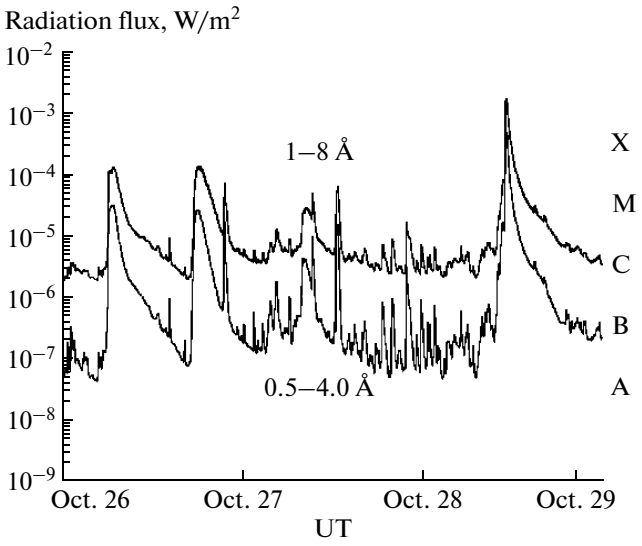

Fig. 8. X-ray fluxes in the 0.5–4 and 1–8 Å channels over the period from October 26 to October 28, 2003, according to the *GOES* data.

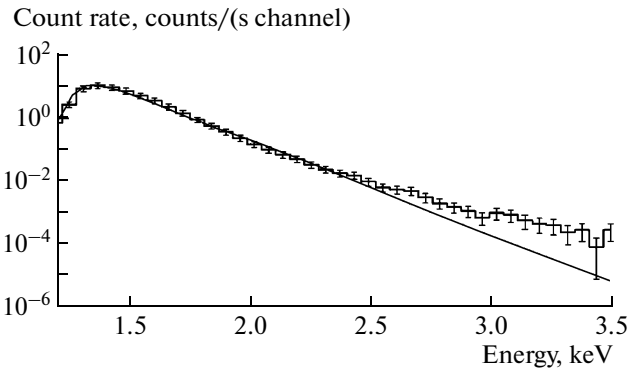

Fig. 9. X-ray spectrum (histogram) of the quiet solar corona obtained using the *SphinX* X-ray spectrophotometer on September 11, 2009. The solid line shows the calculated spectrum corresponding to a temperature of 1.78 ± 0.07 MK [26].

the ranges of 0.5–4 and 1–8 Å by means of the single-temperature model described in Section 4.

From February to November 2009, the *SphinX* X-ray spectrophotometer designed at the Space Research Center in Wroclaw (Poland) [26] operated onboard the *CORONAS-Photon* satellite. The spectrophotometer recorded solar radiation in the photon energy range of 1–15 keV. Four cooled silicon PIN-diodes with 12.7-μm-thick Be input windows capable of operating in the pulse counting mode or the spectral analysis mode were used as detectors. In the pulse counting mode, the sensitivity of the instrument reached 10^{-10} W/m^2, which was two orders of magnitude better than the *GOES* sensitivity. In the spectral analysis mode, the photon energy was determined with an energy resolution of 0.4 keV from the signal amplitude by using a multichannel analyzer. The operation period of the *CORONAS-Photon* satellite coincided with the deep minimum of solar activity in the beginning of the 24th solar cycle; however, even under such an extremely low activity, the *SphinX* spectrophotometer detected a considerable number of weak flares with fluxes much lower than the sensitivity threshold of the *GOES* instrument. As a result, the flare flux scale was extended to two new flare classes lower than class A: class S, corresponding to fluxes of 10^{-9}–10^{-8} W/m^2, and class Q, corresponding to fluxes of 10^{-10}–10^{-9} W/m^2. The *SphinX* spectrophotometer was used to study X-ray emission of flares, active regions, and quiet solar regions. It was found that hot plasma emitting X rays can exist even in the absence of visible signatures of solar activity. Figure 9 shows the X-ray spectrum of the quiet solar corona recorded using the *SphinX* spectrophotometer [26].

At present, several photometers intended to monitor EUV radiation of the solar corona and its time variations associated with solar activity operate in space (Table 3).

The *Solar EUV Experiment* (*SEE*) carried out at the *TIMED* (*Thermosphere Ionosphere Mesosphere Energetics Dynamics*) satellite (United States) [27] includes two instruments: the *XUV Photometer System* (*XPS*), operating in the spectral range of 1–270 Å, and the *EUV Grating Spectrograph* (*EGS*), operating in the range of 270–1940 Å. The *XPS* instrument has nine silicon photodiodes with deposited thin-film filters, which form nine spectral channels with an average resolution of 70 Å. The *EGS* instrument with an effective spectral resolution of 4 Å is built according to the Rowland scheme with a concave diffraction grating and position-sensitive detector on the basis of a multichannel plate with a position-sensitive anode. Both instruments operate for 3 min during each 97-min orbit, which comprises 3% of the total observation time. Over each 3-min time interval, 20 measurements with a time resolution of 10 s are performed. The main goal of this experiment is to monitor X-ray and EUV fluxes from the Sun, which is the main source of heating the Earth's upper atmosphere, and the response of the atmosphere to variations in the solar activity.

The *Large Yield RAdiometer* (*LYRA*) installed at the *PROBA2* (*PRoject for OnBoard Autonomy*) satellite includes four identical units of EUV photometers operating in the spectral ranges of 60–200, 170–800, 1900–2220, and 1200–1230 Å [28]. The first two channels are also sensitive to radiation with wavelengths shorter than 20 and 50 Å, respectively. Silicon photodiodes, as well as diamond-based photodiodes of the MSM and PIN types, are used as detectors. Radiation is continuously recorded by one photometer, the other being used for calibration or special observations. The experiment is aimed at solving the following tasks: measurements of EUV radiation

Table 3. Characteristics of photometers for monitoring EUV radiation of the solar corona

Satellite/instrument	Operating period	Spectral ranges, Å	Spectral resolution, Å	Time resolution, s	Reference
TIMED/SEE	2002–present			10	[27]
XPS		1–270	70	(3% of the total time)	
EGS		270–1940	4		
PROBA2/LYRA	2010–present	60–200	No	0.01	[28]
		170–800			
		1900–2220			
		1200–1230			
SDO/EVE	2010–present				[29]
MEGS-A		50–370	1	10	
MEGS-B		350–1050	1	10	
MEGS-P		1216		0.25	
ESP		1–390	5 channels	0.25	

fluxes with a high (100 Hz) sampling rate, combined comparative observations with other similar instruments (including *TIMED/SEE* and *SDO/EVE*), and tests of novel types of wideband photodiodes on the basis of diamonds.

The *Extreme ultraviolet Variability Experiment* (*EVE*) [29]) intended to study variations in the solar EUV radiation operates at the *Solar Dynamics Observatory* (*SDO*), launched in 2010. The equipment includes several instruments: two *Multiple EUV Grating Spectrographs* (*MEGSs*) with a spectral resolution of 1 Å, operating in the spectral ranges of 50–370 Å (*MEGS-A*) and 350–1050 Å (*MEGS-B*); the *EUV SpectroPhotometer* (*ESP*), measuring the radiation flux in several broad bands in the spectral range of 1–390 Å; and the *MEGS-P photometer,* measuring the radiation flux in the Lα 1216-Å resonance line of hydrogen. As detectors, CCD arrays are used in the *MEGS-A* and *MEGS-B* channels and silicon photodiodes are used in the photometers. The time resolutions of the photometers and spectrographs are 10 s and 0.25 s, respectively. The experiment is aimed at measuring the EUV fluxes with the purpose of forecasting conditions in the Earth's thermosphere and ionosphere, as well as at studying radiation variations caused by solar flares. The observational data will also be used to develop the models of EUV radiation of the transition region and corona of the Sun.

3.2. X-ray Spectrometers and Spectroheliometers

Historically, the first types of instruments for X-ray spectroscopy of the solar corona were simple-design X-ray crystal spectrometers consisting of an input slit or grid collimator, a plane crystal (as a rule, KAP, FDP, or quartz), and a detector (a proportional or Geiger photon counter). Spectral scanning was performed by rotating the instrument as a whole or only the crystal with respect to the direction to the Sun. Such instruments were used in 1970–1995 in the experiments carried out on *Vertical* rockets and *Interkosmos* satellites [30, 31]; the *Solar Maximum Mission* (*SMM*) orbital observatory, equipped with the *X-Ray Polychromator/Flat Crystal Spectrometer* (*XRP/FCS*) [32]; and the *CORONAS-I* and *CORONAS-F* satellites (the *DIAGENESS* (*DIAGnostic of ENErgy Sources and Sinks in flares*) experiment [33], intended to study hot plasma spectra in solar flares and active regions) (see Table 4 [30–37]).

Although these instruments have small dimensions and simple design, their spatial resolution is better than 1' and their spectral resolution in narrow spectral regions in the range from 1.7 to 23 Å is as high as 2×10^3–10^4. Good statistics of the signal provided by these instruments when studying solar flares allowed one to resolve the fine structure of the spectrum in the vicinity of the bright resonance lines of Fe XXIII–XXVI, Mg IX–XI, Si XIII, Ne IX, Ca XIX, and O VIII ions; to determine the electron temperature of flaring plasma from the ratio between the intensities of dielectronic satellites and resonance lines; and to measure the Doppler line widths. Figure 10 shows the solar radiation spectra in two phases of the flare that occurred on November 16, 1970 (the data from the *Interkosmos-4* satellite [30]).

A disadvantage of spectrometers with a plane crystal is the necessity of spectral scanning, which hinders one to achieve the time resolution required to study rapidly varying sources (like flares). This restriction is removed by using Bragg spectroheliometers with concave crystals, in which the required spectral region can be recorded without scanning by using a position-sensitive detector. Such instruments operated onboard the

Table 4. Parameters of high-resolution solar X-ray spectrometers

Satellite/instrument	Operating period	Spectral ranges, Å	Spectral resolution, Å	Reference
Interkosmos-4	1970–1971	1.8–19	4×10^{-4}	[30, 31]
SMM/XSP	1980–1989	1.4–22.4		[32]
FCS			2×10^{-4}–3×10^{-2}	
BCS			$(1.8–6.2) \times 10^{-4}$	
Yohkoh/BCS	1991–2001	1.76–1.80,	3.8×10^{-4}	[34]
		1.82–1.89	5.3×10^{-4}	
		3.16–3.19,	5.3×10^{-4}	
		5.01–5.11	1.86×10^{-3}	
CORONAS-F/DIAGENESS	2001	3–7	$(1–4) \times 10^{-4}$	[33]
CORONAS-F/RESIK	2001–2003	3.3–6.1	8×10^{-3}–1.7×10^{-2}	[35]
CORONAS-F/PEC(MgXII)	2001–2003	8.41–8.43	10^{-3}	[37]

SMM (the *Bragg Crystal Spectrometer* (*BCS*) [32]), *Yohkoh* (BCS [34]), and *CORONAS-F* (the *RESIK* SXR spectrometer [35]) satellites.

A specific feature of crystal X-ray spectrometers is that their field of view is as small as several tens of arc seconds. The field of view is determined by the width of the reflection curve of the crystal and is limited by the collimator. Objects lying beyond the field of view are recorded consecutively by rotating the instrument or satellite as a whole, which results in time delays between records up to several tens of seconds. When studying fast processes, such as flares, the coronal structure under study should be simultaneously recorded in several spectral lines with the best time resolution. The problems of identification of X-ray spectral lines of the Sun were considered in [36].

To obtain an image of the entire Sun in the Mg XII 8.42-Å line, an REC X-ray imaging Bragg spectroheliograph was designed at the Lebedev Physical Institute (LPI), Russian Academy of Sciences (Moscow). Such instruments were used at the *CORONAS-I* and *CORONAS-F* satellites as components of the *SPIRIT* complex [37, 38]. A thin quartz crystal (with a lattice parameter of $d = 8.501$ Å and dimensions of 60 × 40 mm) fixed on a spherical substrate with a curvature radius of 1295 mm produced an image of the entire Sun in the 8.41 + 8.43 Å doublet of Mg XII ions. The image was recorded using a 1024 × 1152 windowless CCD array with 13 × 13-μm cells (Fig. 11). The time resolution was 30 s for full-frame images and 7 s for images recorded in the reduced field of view. At a nearly normal (8°) diffraction angle, the focal length of the mirror was 654 mm, the angular resolution was

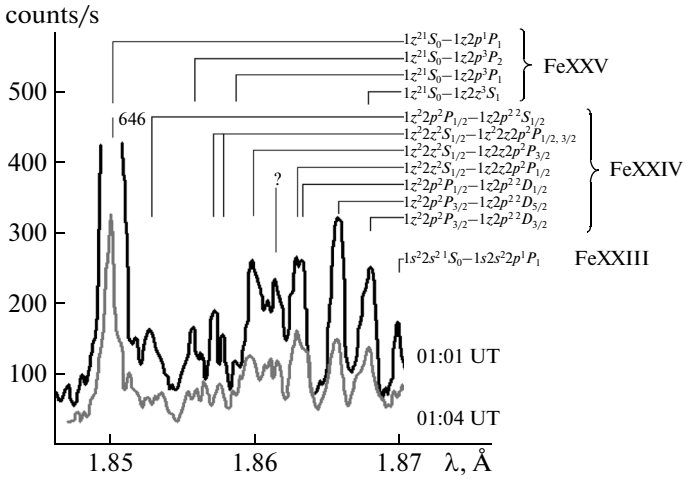

Fig. 10. Spectrum of the solar flare (November 16, 1970) in the Fe XXIII–Fe XXV lines in the spectral range of 1.84–1.88 Å taken using an X-ray spectrometer installed at the *Interkosmos-4* satellite [30].

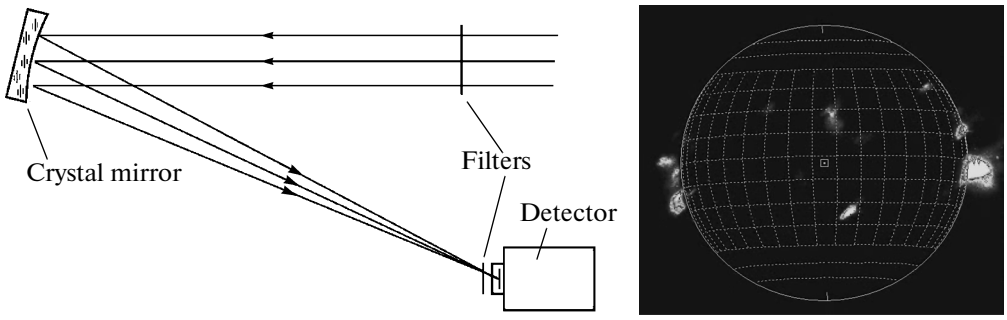

Fig. 11. Scheme of the *RES* Mg XII spectroheliograph of the *SPIRIT* complex installed at the *CORONAS-F* satellite and image of the Sun in the Mg XII 8.42-Å line obtained on January 18, 2002.

4.1″, and the spectral resolution in the dispersion plane was 1.2×10^{-3} Å. A specific feature of this optical scheme is that radiations with different wavelengths diffract on different annular zones of the mirror. Exact focusing is possible only for one wavelength, while the images of a point source in other wavelengths have the shapes of arc segments. Due to the high resolution of the detector and small aberrations, the instrument allows one to resolve the components of the Mg XII doublet in the image and measure their Doppler widths at a temperature of about 5 MK [39].

3.3. Wideband X-ray Telescopes and Spectrometers

The sources of X-ray emission in the solar corona are associated with local magnetic field concentrations. Experimental studies of these sources are usually aimed at solving the following two types of tasks:

(i) determination of the spatial location of quasi-stationary radiation sources and their relationship with the magnetic field structure and measurements of the characteristic parameters and long-term dynamics of the plasma;

(ii) localization of fast local variations in the radiation intensity associated with spontaneous activity (such as flares and CMEs) and determination of their physical mechanisms.

The first task requires instruments capable of recording images in a wide field of view with a sufficiently high angular resolution and low time resolution. For the second task, it is necessary to take images in a relatively narrow field of view, but with high spatial and high time resolutions. None of these tasks requires high spectral resolution.

Two types of instruments with high angular and high time resolutions and a moderate spectral resolution were designed to study X-ray emission of the solar corona: grazing incidence mirror telescopes with CCD image detectors for the SXR band and telescopes-spectrometers with modulation collimators and position-sensitive semiconductor detectors for the hard X-ray (HXR) band. The spectral resolution of X-ray reflecting telescopes is provided by filters. The spectral resolution of modulation telescopes is achieved owing to the sensitivity of detectors to the photon energy.

The first grazing incidence mirror telescopes of the S-054 and S-056 types operating in the spectral ranges of 3.5–47 Å [40] and 3–60 Å [41], respectively, and recording images on a film worked at the *Skylab* orbital station in 1973–1974. The *SXR Telescope* (*SXT*) onbord the *Yohkoh* satellite launched in 1991 [42] operated in the spectral range of 3–45 Å. Due to the more perfect optics and the use of a CCD detector, this telescope had much higher angular (3″) and temporal (to 10 s) resolutions. The use of five filters made of Al, Be, and Mg foils with different thicknesses allowed one to select narrower temperature intervals from the entire 1–8 MK sensitivity range of the telescope, which made it possible to determine the differential emission measure (DEM) function of the solar plasma from the signal ratio with an accuracy of up to 0.1 MK.

The next modification of this instrument is the *X-Ray Telescope* (*XRT*) designed for the *Hinode* satellite [43] and operating from 2006 up to the present time. The angular resolution of the XRT is about 1″. The telescope has a set of filters on the basis of Al, C, Ti, and Be films with different thicknesses deposited on polyimide substrates or fixed on fine grids. This allows one to analyze the temperature structure of plasma radiation in the range from 0.5 to 10 MK, which covers both the quiet and active solar corona conditions.

In modulation telescopes, the HXR image of the Sun is recovered mathematically by analyzing spatial modulation of the signal from the position-sensitive detector exposed through the collimator grids, which create a moire pattern. The *RHESSI* (*Reuven Ramaty High-Energy Solar Spectroscopic Imager*) telescope [44, 45] launched in 2006 operates in the photon energy range from 4 keV to 17 MeV. It has nine collimators consisting of grids with different periods and placed at the distances of up to 1.5 m from one

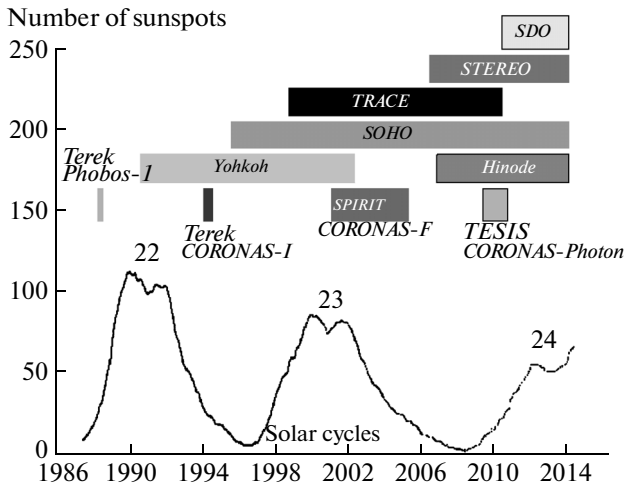

Fig. 12. Experiments on studying the solar corona by means of X-ray and EUV telescopes. The lower plot shows the time evolution of the number of sunspots (which quantitatively characterizes the solar activity) in the 22nd, 23rd, and 24th solar cycles.

another. Behind the collimator, there is a cooled segmented Ge detector, the signal from which is modulated with the satellite rotation frequency (one turn per 4 s). The maximum angular resolution of 2.3″ in the field of view of up to 1° is determined by the minimum grid period. For a sufficiently bright source (such as a flare), one half-rotation is sufficient to construct a source image with a time resolution of better than 0.1 s. The best spectral resolution of the detector is 1 keV.

3.4. Spectrally Selective EUV Telescopes with Multilayer Optics

Spectrally selective EUV telescopes are the main type of instruments for studying the solar corona in a wide range of temperatures (from a few hundred thousands of kelvins to 10–20 MK) with high spatial resolution. To date, ten instruments of this type were launched (Fig. 12). Historically, the first telescope of this type was the *TEREK* X-ray telescope-coronograph designed at the LPI for the *Phobos-1* spacecraft launched in 1988 [46]. From the mid-1990s, telescopes of this type were launched regularly and became the main type of instruments for studying and monitoring the solar corona. They include the following telescopes: *CORONAS-I/TEREK-K* (1994 [47]), *SOHO/EIT* (*SOlar and Heliospheric Observatory/EUV Imaging Telescope,* from 1995 up to the present [48]), *TRACE* (*Transition Region And Coronal Explorer,* 1996–2011 [49]), *CORONAS-F/SPIRIT* (*Spectrometric Imaging Roentgen Telescope,* 2001–2005 [50]), two *STEREO/EUVI* (*Solar TErrestrial RElations Observatory/Extreme Ultra-Violet Imager*) telescopes (A and B, from 2006 up to the present [51]), *CORONAS-Photon/TESIS* (*TElescope–Spectrometer for Imaging Spectroscopy,* 2009 [52]), *PROBA2/SWAP* (*PRoject for Onboard Autonomy/Sun Watcher using Active pixel system detector and image Processing,* from 2009 up to the present [53]), and *SDO/AIA* (*Solar Dynamic Observatory/Atmospheric Imaging Assembly,* from 2010 up to the present [54]).

The main difference between spectrally selective and grazing incidence telescopes is that the former use normal incidence optics with spectrally selective coatings optimized for measurements in a narrow spectral band containing the brightest lines (or a group of lines) of iron ions in different charge states corresponding to different characteristic plasma temperatures. Telescopes with multilayer optics operate in the EUV band of 94–335 Å and usually have two, four, or more spectral channels with a resolution of $\lambda/\Delta\lambda \sim 10$–$20$ operating alternately or simultaneously. As an example, Table 5 presents the wavelengths of the spectral lines recorded by the channels of the *SDO/AIA* telescope and Fig. 13 shows the temperature response functions of these channels [54].

The spectral selectivity of the mirrors is provided by depositing multilayer interference coatings of a pair of materials with different values of the dielectric constant $\varepsilon(\lambda)$ and a period close to $\lambda/2$ on substrates with super-smooth surfaces (with an r.m.s. roughness of less than $\lambda/40$, i.e., 2–8 Å). The number N of efficiently reflecting pairs of layers is determined by the radiation attenuation inside the structure; in this case, the spectral resolution is $\lambda/\Delta\lambda \sim N$ [55, 56]. Figure 14 shows the single-reflection function of the multilayer coating of the T1-171, T1-195, T1-284, and T1-304 channels of the *SPIRIT* telescope [50]. At normal incidence, the maximal reflection coefficient in the range of 171–304 Å is achieved for a pair of Mo–Si layers (the theoretical maximum of ~70% corresponds to $\lambda = 171$ Å). Most of modern EUV telescopes employ double-mirror Ritchey–Chretien systems having a higher resolution and coatings with a large number of optimized layers. In this case, the reflection coefficient remains high, while the spectral width of reflection decreases by a factor of 1.5–2 [52].

To suppress visible radiation of the Sun and the long-wavelength wing of the reflection function, filters are installed in front of the input window of the telescope and directly in front of the detector. Depending on the required spectral transmission of the channel [57, 58], aluminum (the range of 171–350 Å) or other metal films deposited on grids or polymer substrates are used as filters.

A wide scope of problems associated with studying the structure of the solar corona and its dynamics in the total range of coronal temperatures have been solved using spectrally selective EUV telescopes. Spatial superimposition of the images of coronal structures taken at the close instants of time in different temperature channels makes it possible to study the temperature distribution over the solar atmosphere

Table 5. Wavelengths of spectral channels, major ions contributing to radiation, their specific temperatures, and types of coronal structures observed by the *SDO/AIA* telescope [54]

Channel	Major ions contributing to radiation	Maximum emission temperature, $\log_{10}(T\,[\mathrm{K}])$	Characteristic solar structure
4500 Å	Continuum	3.7	Photosphere
1700 Å	Continuum	3.7	Photosphere
304 Å	HeII	4.7	Chromosphere, transition region
1600 Å	CIV + continuum	5.0	Transition region, upper photosphere
171 Å	FeIX	5.8	Quiet corona, transition region
193 Å	FeXII, XXIV	6.2, 7.3	Corona, flares
211 Å	FeXIV	6.3	Active regions
335 Å	FeXVI	6.4	Active regions
94 Å	FeXVIII	6.8	Flares
131 Å	FeVIII, XXI	5.6, 7.0	Transition region, flares

layers, trace the dynamics of the temperature and spatial variations in the coronal structures, and determine physical mechanisms for the heating and dissipation of plasma energy. Such method of analysis—X-ray and EUV imaging spectroscopy of the solar corona, extensively developed in experiments carried out on *CORONAS* satellites [38]—has demonstrated its high efficiency in studying various coronal structures, such as ARs, solar flares, and CMEs [59].

3.5. EUV Diffraction Spectrometers

There are two types of solar EUV diffraction spectrometers: spectrometers with a slit and slitless spectroheliometers.

Slit spectrometers are characterized by high spectral and spatial resolutions, but have a very small field of view (several arc minutes) determined by the width of the input slit. Pointing the instrument at the solar disk region under study and scanning small areas of the Sun's surface are provided by rotation of the primary focusing mirror (grazing or normal incidence) or internal scanning mirrors. The parameters of solar diffraction slit spectrometers are given in Table 6.

The program of studies of solar spectra with the use of the *SERTS* (*Solar EUV Rocket Telescope and Spectrograph*) rocket spectrometer included five launches performed in 1989, 1991, 1993, 1995, and 1997. The last experiment was described in [60]. The main goal of this experiment was to measure the wavelengths and

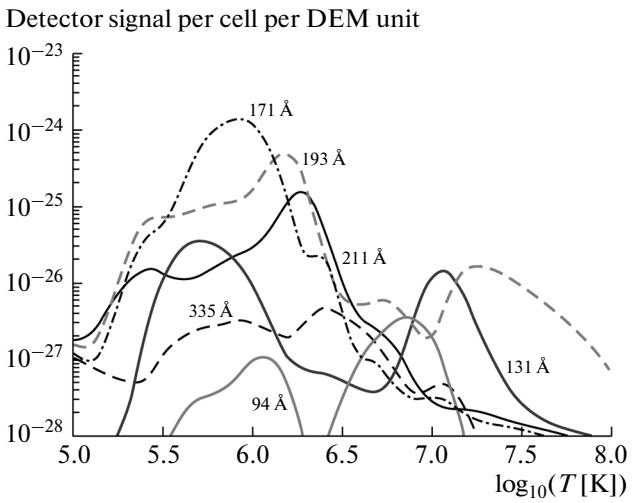

Fig. 13. Transmission coefficient (detector signal per cell per DEM unit) of the *SDO/AIA* telescope as a function of the temperature for different wavelengths [54]. Here, DEM unit = 1 $\mathrm{cm}^5\,\mathrm{s}^{-1}$.

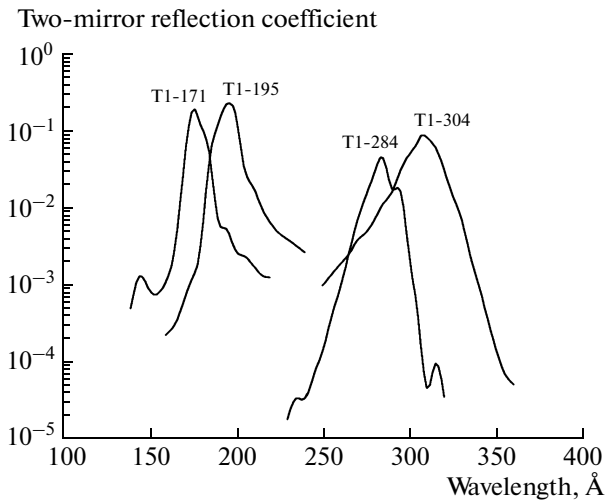

Fig. 14. Spectral functions of reflection of the *T1-SPIRIT* multilayer mirror telescope [50].

Table 6. Parameters of diffraction EUV spectrometers with slits

Instrument (spacecraft, operating period)	Spectral ranges, Å	Field of view (without scanning/with scanning)	Angular resolution, arcsec	Spectral resolution, Å	Reference
SERTS (rocket, 1997)	299–353	3′ × 8.5′	7	0.115	[60]
CDS (*SOHO*, 1996–2013)	151–785	4′	2	0.21	[61]
	308–381	Entire disk (scan)		0.08	
	513–633			0.14	
SUMER (*SOHO*, 1996–2012)	465–1600	4″ × 5′ (slit)	1	0.045–0.023	[62, 63]
		Entire disk (scan)			
EIS (*HINODE*, 2006–present)	170–210, 250–290	6′ × 8.5′, shift up to 15′	1	0.05	[64]

intensities of spectral lines in a given region of the EUV band with an accuracy required for comparison with theoretical atomic data and diagnostics of the plasma of individual solar structures (in the earlier experiments, the spectra of the entire Sun were measured). All instruments of this series were built according to the scheme of a stigmatic slit spectrograph with a toroidal diffraction grating and differed only in the types of detector and grating coating. The results obtained in the *SERTS* experiment were used in developing the CHIANTI software package [21] for calculating the line intensities of the EUV band and the method of plasma diagnostics by means of the DEM function.

The Coronal Diagnostic Spectrometer (CDS) [61] is installed at the *SOHO* observatory launched into Lagrange point L1 in December, 1995. The parameters of the instrument were determined by its scientific goals consisting in plasma diagnostics of various solar structures with high spatial, temporal, and spectral resolutions. The spectral range included the lines of the upper chromosphere, transition region, and solar corona excited at temperatures from 10^4 to 10^6 K. The spectral and spatial resolutions allowed one to distinguish closely spaced lines in the spectral range of 150–200 Å in solar structures with different temperatures, which made it possible to perform local plasma diagnostics. The instrument is a two-band diffraction spectrometer with one grazing incidence mirror. It has two channels: a grazing incidence spectrometer (GIS) operating in the spectral range of 150–785 Å and a normal incidence spectrometer (NIS) operating in the ranges of 308–381 and 513–633 Å. The GIS detector is a multichannel plate (MCP) with an integral anode operating in the pulse counting mode. The NIS detector is a CCD array with an MCP intensifier. The accuracy of absolute calibration of the instrument is 20%. Among the most important results obtained the CDS, it is worth noting measurements of the fine structure of ARs and small-scale solar structures, study of their relationship with the magnetic field configuration, and study of the processes of plasma heating in ARs and flares.

The *SUMER* (*Solar Ultraviolet Measurements of Emitted Radiation*) high-resolution spectrometer is also installed at the *SOHO* observatory [62, 63]. The instrument is a stigmatic spectrograph operating in the spectral range of 465–1600 Å. It has a parabolic primary mirror, a concave normal incidence grating, and two MCP detectors with coordinate detection of the signal. The spectral resolution varies from 0.0447 Å in the first order at the wavelength of 660 Å to 0.0206 Å in the second order at the wavelength of 1500 Å. Due to its high spectral resolution, the spectrometer can be used to study the profiles of spectral lines and reveal their nonthermal broadening (i.e., that exceeding their Doppler widths at the corona temperature) caused by plasma turbulence or macroscopic plasma motion. Although the *SOHO* observatory was launched more than 17 years ago, almost all its instruments continue to operate, though with a smaller numbers of session.

In 2006, the *EUV Imaging Spectrometer* (*EIS*) [64] spectrometer was launched onboard the *Hinode* satellite (Japan). This instrument is aimed at studying the emission spectra of the solar corona and the transition layer in the spectral ranges of 170–210 and 250–290 Å. Due to its significant effective area and high angular resolution, the spectrometer allows one to analyze the profiles of spectral lines, determine the Doppler shift related to plasma drift with a velocity of higher than 5 km/s, and measure the nonthermal component of the line broadening. The instrument can operate in several modes, including scanning of solar regions with dimensions of several arc minutes in up to 25 spectral lines. It allows one to simultaneously measure the line profiles and study variations in the intensities of several chosen lines in a given field of view with a time resolution of 1 s. The spectrometer design includes a primary mirror with a multilayer coating, a unit for changing the slits and scanning, a toroidal grating with a multilayer coating, and two CCD detectors. The temperature range covered by the

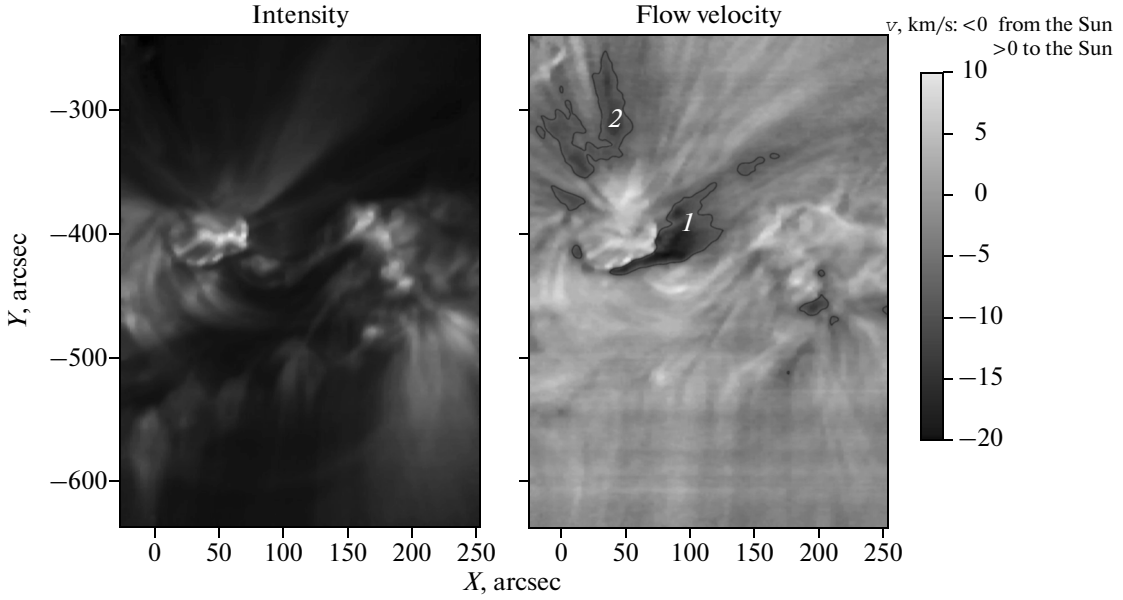

Fig. 15. Intensity map in the Fe XII 195-Å line (on the left) and Doppler velocity map (on the right) determined from the width of this line in the AR image obtained using the *Hinode/EIS* spectrometer on October 15, 2010. Scales on the abscissa and ordinate show the distance (in arc seconds) from the center of the Sun. Numbers *1* and *2* indicate regions of plasma outflow with a velocity of about 10 km/s.

recorded spectral lines is $\log_{10}(T\,[\mathrm{K}]) = 4.7–7.3$. The scientific goals of this experiment are to measure the plasma drift velocity in ARs and individual magnetic loops, investigate the processes of plasma heating in ARs, perform coronal seismology by means of the Doppler shifts, reveal mechanisms for the initiation and kinematics of flares and CMEs, and study transient events. A typical intensity map of an AR in the Fe XII 195-Å line and the map of plasma velocities determined from the Doppler width of this line are shown in Fig. 15. The numbers *1* and *2* indicate the regions from which plasma outflows with a velocity of about 10 km/s.

Slitless EUV spectroheliographs with a normal or grazing incidence diffraction grating record the spectrum in the form of monochromatic solar images in separate spectral lines focused onto the detector plane. If the distance between neighboring images, which is determined by the grating dispersion, is less than the angular solar size, then these images are partly superimposed. In the case of the strongest spectral lines or bright point objects like flares, this disadvantage of the slitless scheme does not present a serious problem and is requited by the possibility of simultaneously obtaining the spectrum of the entire Sun with a high spatial resolution. The first instrument of this type was the *S-082A* spectroheliograph installed at the *Skylab* station [65]. Using the spherical diffraction grating with a focal length of 4 m, the spectrum in the range of 170–630 Å was focused on the film in the form of monochromatic solar images with a diameter of 18 mm, which corresponded to a 25-Å wavelength interval. The spectral resolution determined from the lines of the Lyman series of He^+ was 0.15 Å, and the angular resolution in the image was 5″.

The *SPIRIT* complex installed at the *CORONAS-F* satellite included the *RES-C* X-ray spectroheliograph [38], which contained two slitless XUV spectroheliographs operating in the spectral ranges of 176–207 and 280–330 Å. Both instruments had plane grazing incidence gratings with a groove density of 3600 grooves/mm at their entrances. A normal incidence spherical mirror with a multilayer coating and focal length of 830 mm was used for spectrum focusing in the 176–207 Å channel, and a parabolic mirror with a focal length of 570 mm was used in the 280–330 Å channel. 1024 × 1152 CCD arrays with optoelectronic image intensifiers were used as detectors. The main parameters of the *RES-C* spectroheliographs are given in Table 7, and the solar spectrum recorded using this instrument is shown in Fig. 16. Since the grazing angles are less than the diffraction angles, the solar images are compressed in the dispersion direction by a factor equal to the ratio between the sines of the diffraction and grazing angles (by nearly 18 times). This scheme is very convenient to study the flare spectra, because the flare regions are small in size and the brightest flaring lines are well distinguished, being on one line of sight against the background spectrum of the quiet Sun.

Table 7. Parameters of spectral channels of the *RES* XUV spectroheliograph

Spectral range, Å	176–207	280–330
Grazing angle, deg	1.16	1.40
Diffraction angle for λ_{av}, deg	21.46	27.36
Spectral resolution, Å /cell	0.024	0.043
Spectral distance between separated solar images, Å	0.44	0.52
Spatial resolution in the direction perpendicular to dispersion, arcsec/cell	5.4	7.9
Spatial resolution in the dispersion direction, arcsec/cell	97.5	148.6

3.6. Trends in Progress of Space Instruments for Spectroscopic Studies of the Solar Corona

Spectroscopic studies of the Sun onboard spacecraft, which have been performed since the end of 1950s, have laid the foundation for the actively developing physics of the solar corona. The obtained results have demonstrated the complexity and interrelation of solar events and the variety of the physical processes occurring on different spatiotemporal scales. The problems of studying moderate-scale coronal structures (from several hundred kilometers to several solar radii), diagnostics of their state, and description of the phenomena occurring in them have largely been solved using the instruments described above. Nevertheless, many fundamental problems of solar physics, such as the heating of the solar corona, the nature of solar activity, and the origin and acceleration of the solar wind, remain challenging up to the present. Attempts to simulate and forecast the phenomena occurring in the corona (e.g., to predict flares or CMEs) do not provide the desired accuracy. To a certain extent, this is associated with the most important, but still unresolved, problem of measuring and simulating the coronal magnetic fields. The other reason is the lack of data on the processes occurring on small spatial (from several to a few tens of kilometers) and temporal (fractions of a second) scales, which can play an important role in creating physical conditions and developing magnetoplasma processes in the solar corona.

The nearest (for 5–10 years) prospects in the development of experimental studies of the solar corona are associated with studying small-scale phenomena and clarifying their role in the genesis of large-scale and global processes of solar activity and the formation of heliospheric conditions. The scope of these problems includes studies of small-scale magnetoplasma structures with a spatial resolution better than 200 km (at present, a resolution of ~450 km is achieved using the *SDO/AIA* telescope), search for the acceleration mechanisms of the solar wind and charged particle beams, observations of magnetic reconnection regions in flares and CME precursors, and studies of small-scale solar activity and its influence on the characteristics of the heliosphere.

To solve the above problems, it is necessary to develop a new generation of instruments for studying the corona with higher spatial, temporal, and spectral resolutions. Two approaches to solving this problem are presently being developed. The first approach, implemented in such large projects as the *Solar Orbiter* of the European Space Agency [66] and the *Intergelioprobe* of the Russian Space Agency [67], suggests studies of small-scale structures and phenomena from the minimum possible distance from the Sun. Thus, the *Solar Orbiter* and *Intergelioprobe* spacecraft will be launched into the solar orbits with perihelions of 60 and 40 solar radii, respectively. EUV and X-ray telescopes and spectrometers, as well as instruments for in situ measurements of the parameters of space plasma and solar wind, will be installed at these spacecraft, which will allow one to observe the influence of solar processes on the formation of space environment directly in the heliosphere.

The second approach uses the latest advances in space instrument engineering and technology to increase the resolution of instruments launched into near-Earth orbits as much as possible. In June 2013, the *IRIS* (*Interface Region Imaging Spectrograph*) [68] ultrahigh-resolution EUV telescope/spectrometer was launched in the framework of the *SMEX* (*SMall Explorer*) small-satellite program (NASA, United States). This instrument is aimed at studying the chromosphere and the transient region between the photosphere and the corona with an angular resolution of 0.33″–0.4″ (0.16″ per detector cell) and a time resolution of 1–2 s. The spectral resolution is sufficient to reveal plasma flows with velocities on the order of 1 km/s. The spatial and spectral resolutions of the *IRIS* telescope are several times higher than those of similar instruments, such as *SUMER* and *EIS*.

At present, the *Solar-C* project of the Japanese Aerospace Exploration Agency Studies [69] is under development. In this project, it is planned to use three ultrahigh-resolution telescopes/spectrometers operating in the visible, EUV, and X-ray spectral bands. The characteristics of instruments for spectroscopic studies of the Sun in the X-ray and EUV bands that are presently being developed in the frameworks of the most advantageous space projects are given in Table 8.

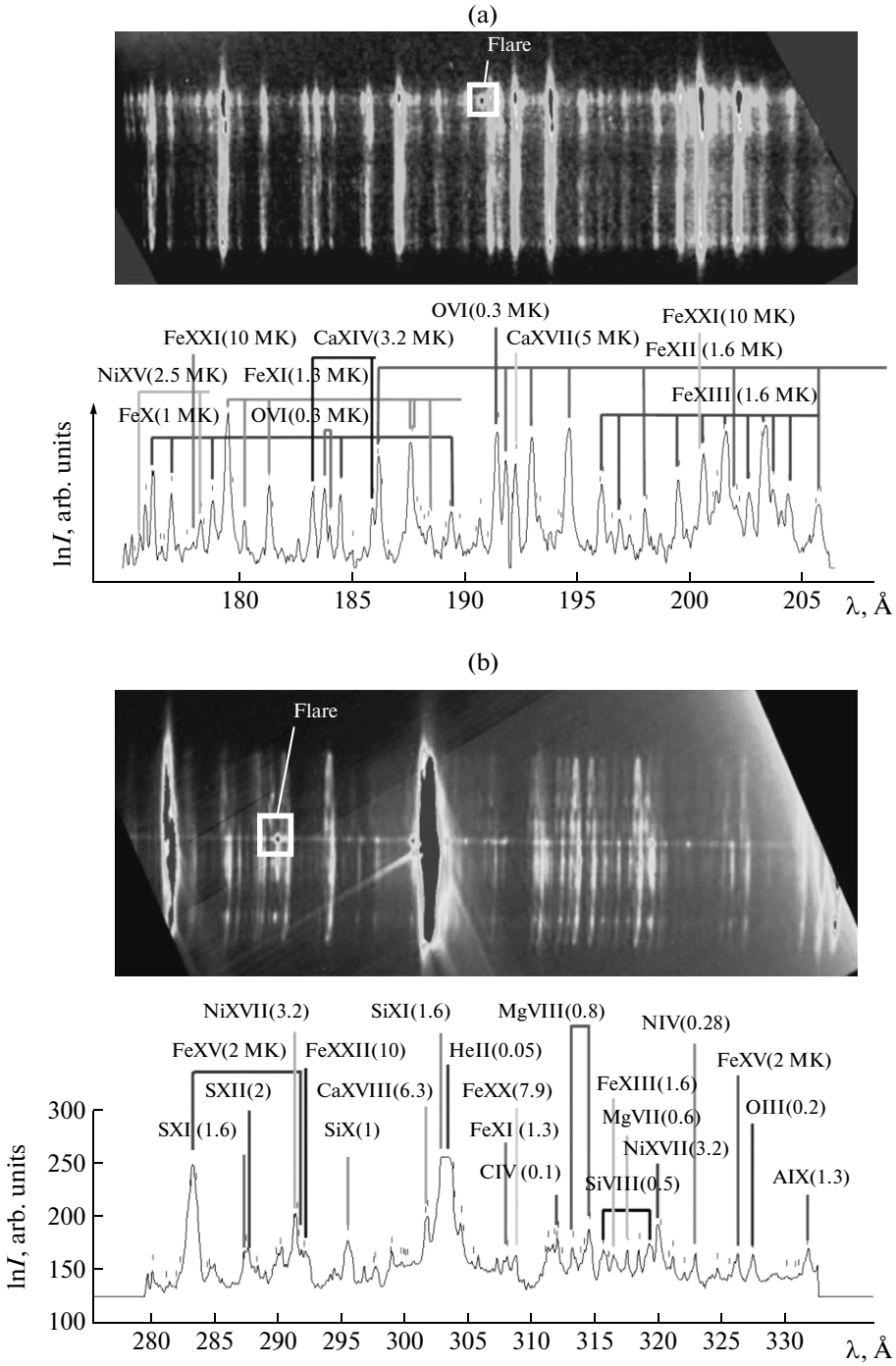

Fig. 16. Spectral images of the Sun obtained on 03 : 59 UT September 16, 2001, in the (a) 176–207 and (b) 280–330 Å channels of the *RES* (*SPIRIT)* XUV spectroheliograph [38].

4. TEMPERATURE AND DENSITY DIAGNOSTICS FOR ANALYZING SOLAR CORONAL STRUCTURES

Spectroscopic diagnostics of plasma sources is based on the sensitivity of the recorded radiation spectra to physical conditions in plasma. Since the observed radiation is integrated along the line of sight, it is necessary, in general, to solve the spectral inverse problem in order to obtain information on the local plasma parameters from the observed spectra. This problem refers to the class of ill-posed problems; therefore, in the general case, it cannot be formulated and solved without additional assumptions on the state of the object under study. Thus, when formulating the

Table 8. X-ray and EUV spectral instruments developed for prospective space missions

Project (year of launching)	Instrument	Spectral range	Reference
Solar Orbiter (2018)	*EUI* EUV telescope *SPICE* imaging spectrometer *METIS* telescope-coronagraph-polarimeter *STIX* X-ray telescope-spectrometer	174, 304, 335 Å 485–525, 702–792, 972–1050 Å HLα 1216 Å, HeII 304 Å, vis. 4–150 keV [66]	[66]
Interhelioprobe (after 2020)	*Trek* X-ray imaging spectrometer *Sorento* Solar X-ray imaging telescope *ChemiX* X-ray spectrometer *Helicon-I* scintillation gamma-spectrometer	132; 171; 304; 8.42 Å 5–100 keV 1.3–8 Å 10 keV–15 MeV	[67]
IRIS (launched in June 2013)	*IRIS* high resolution EUV telescope/spectrometer	1332–1358, 1389–1407, 2783–2834 Å	[68]
Solar-C (2020)	*SUVIT* solar telescope *EUVST* spectroscopic telescope *XIT* X-ray telescope/spectrometer	IR, visible, EUV 17–21, 69–85, 92.5–108.5, 111.5–127.5, 46–54, 56–64 nm 0.5–10 keV 94, 171, 304 Å	[69]

inverse problem, the plasma state is determined by the entire existing information on the radiation source with additional assumptions required to form a basis of the physical plasma model. Direct comparison of the recorded ion emission spectra with those calculated using such models allows one to determine the plasma parameters; estimate the confidence level of the adopted assumptions on the conditions in the emitting region; and, thereby, choose the adequate model.

To solve the main problem of spectroscopy, namely, to identify and interpret the line spectra of the coronal plasma, it is necessary to know a large number of atomic characteristics, as well as to have information on the characteristics of the sources. On the other hand, having reliably identified spectra, it is possible to construct models of emitting plasma and, with their help, to determine the plasma macroparameters, such as the spatial distributions of the temperature, density, and ion composition, as well as other plasma characteristics and their time evolution, i.e., to solve the other problem of spectroscopy—plasma diagnostics.

In this section, we consider some methods of spectroscopic diagnostics that are used to study plasma structures of the solar corona. In Sections 4.1 and 4.2, we consider coronal plasma models and diagnostic methods based on the use of the spectral line intensities. As an example, in Section 4.3, we present results of studies and diagnostics of hot coronal structures on the basis of the data obtained in the *SPIRIT* experiment carried out onboard the *CORONAS-F* satellite. In the subsequent sections, we consider methods and results of the diagnostics of various coronal structures, such as the extended solar corona (Section 4.4), QRs and CHs (Section 4.5), and eruptive events (Section 4.6).

4.1. Spectroscopic Coronal Plasma Models (Single-Temperature Model, Multitemperature Model, and DEM)

The following models of emitting plasma are used to describe solar spectra and construct the synthetic spectrum: the single-temperature (ST) (or isothermal) model, the multitemperature (MT) model, and the nonthermal (NT) electron model. In the ST model, the plasma temperature is assumed to be uniform over the studied volume, whereas the MT model assumes that there are several plasma components with different temperatures. In the NT model, the electron velocity distribution function (EVDF) is assumed to be non-Maxwellian and contain an admixture of suprathermal (in the general case, nonisotropic) electrons.

Two main approaches can be used to determine plasma characteristics from the emission spectra: the ab initio approach and the semiempirical one, which is based on the solution of the inverse problem of spectroscopy. In the first approach, the theoretical spectra obtained by numerically simulating plasma processes are compared with experimental data and the adequacy of the plasma model is judged from the degree to which they coincide. In this approach, the plasma characteristics are determined by solving the corresponding equations of plasma dynamics. In the semiempirical approach, the theoretical (also called synthetic) spectrum is constructed using models of emitting plasma. The parameters of these models are the plasma characteristics to be determined by comparing with the measured spectrum. For example, the notion of the "measured" plasma temperature has the sense only in isothermal models, which assume that the EVDF is Maxwellian and there are no temperature gradients in plasma. In this case, the method of suc-

cessive approximations is used. The primary analysis is performed and the spectra are identified by means of the simplest models with the minimum possible number of free parameters (e.g., the ST model). If the difference between the calculated synthetic spectrum and the experimentally determined spectrum exceeds the measurement error, then multiparametric models (e.g., the MT model with or without the allowance for nonthermal electrons) with parameters refined at each iteration step are used until the required agreement with experiment is achieved.

One of the widespread concepts used in the diagnostics of coronal plasma is the notion of the DEM, which was apparently introduced for the first time in [70] and is related to the spatial plasma characteristics, such as the electron density and temperature. To define the DEM, let us write the population of the upper level of emitting ions in the form of the product

$$N(X_i^{+m}) = \frac{N(X_i^{+m})}{N(X^{+m})}\frac{N(X^{+m})}{N(X)}\frac{N(X)}{N(H)}\frac{N(H)}{N_e}N_e, \quad (4.1)$$

where $N(X^{+m})$ is total ion population in the charge state $+m$, $N(X)$ is the abundance of the element X, and $N(H)$ is the abundance of hydrogen in plasma. Using Eq. (4.1), we define the function $G(T, N)$ as

$$G(T_e, N_e) = \frac{N(X_i^{+m})}{N(X^{+m})}\frac{N(X^{+m})}{N(X)}\frac{N(X)}{N(H)} \times \frac{N(H)}{N_e}\frac{A_{ik}}{N_e}\ (\text{photon cm}^3\ \text{s}^{-1}). \quad (4.2)$$

Hence, expression (1.3) for the radiation flux in the lth spectral line takes the form

$$I_l = \frac{1}{4\pi R^2}\int_V G_l(T_e(\mathbf{r}), N_e(\mathbf{r}))N_e^2(\mathbf{r})dV, \quad (4.3)$$

where $T_e(\mathbf{r})$ and $N_e(\mathbf{r})$ are three-dimensional distributions of the electron temperature and density in the plasma volume V, respectively, and the function G_l is the spectral emissivity normalized to one atom and one electron, usually called in the astrophysical literature the contribution function (see, e.g., [2]).

The quantity $dY = N_e^2 dV$ (in units of cm^{-3}), which has the meaning of the amount of emitting plasma contained in the volume element dV and is called the emission measure (EM) of this volume, depends on the state of plasma. The total EM in the volume V (or the volume EM) is defined as the integral $Y = \int_V N_e^2 dV$.

Under steady-state conditions, the radiation source is characterized by a certain temperature distribution $T_e(\mathbf{r})$ over the volume V. The volume can be defined as a function of the temperature $V(T)$; in this case, the density N_e will be characterized by the same temperature in this volume. Then, the DEM $y(T)$ can be defined as a function of the temperature via the expression

$$y(T)dT = \left\langle N_e^2 \right\rangle_T dV, \quad (4.4)$$

where $\left\langle N_e^2 \right\rangle_T$ is the mean square of the electron density over all volume elements dV_i at a temperature T ($dV = \sum_i dV_i$) inside the entire volume V. The DEM function $y(T)$ (in units of $\text{cm}^{-3}\ \text{K}^{-1}$) defined in this way describes the distribution of the emitting substance as a function of the temperature and allows one to study the temperature composition of plasma structures. In the low-density coronal plasma, there are many lines the contribution functions G_l of which are practically independent of the plasma density. For such lines, expression (4.3) takes the form

$$I_l = \frac{1}{4\pi R^2}\int_V G_l(T)y(T)dT, \quad (4.5)$$

where we used the notation $G_l(T)$ for the function independent of N_e. The strict determination of the DEM (including the general case of the DEM as a function of the temperature and density) can be found in [71–73]. The mathematically correct determinations of the EM and DEM via the Stieltjes integral are given in [74, 75].

Thus, the model of emitting plasma under the steady-state conditions of the optically thin coronal plasma can be formulated in terms of the convolution of the contribution function $G_l(T)$ and the DEM function $y(T)$. The first factor of the convolution is determined from the emissivity functions, which are computed under the adopted model assumptions. The last factor, $y(T)$, is determined by solving the inverse problem with a given spectrum $I(\lambda)$ obtained from measurements. The problem of finding the function $y(T)$ is then reduced to solving a set of integral equations of form (4.3) and (4.5) for a properly selected set of spectral lines. Figure 17 shows typical DEM distributions for CHs, QRs, and ARs from the CHIANTI database [21].

4.2. Determination of the Coronal Plasma Parameters from Spectral Line Intensities

Diagnostic methods based on measurements of the relative intensities of spectral lines are widely used to determine the coronal plasma parameters, such as the electron temperature and density, ion temperature, and ion composition. This is done by comparing the theoretical spectra calculated in the framework of certain models with the results of measurements. The best accuracy is provided by the ratios of the line intensities of the same ion, because, in this case, this ratio does not depend on the relative abundances of different chemical elements and the ion composition of the same element, but is determined by the populations of

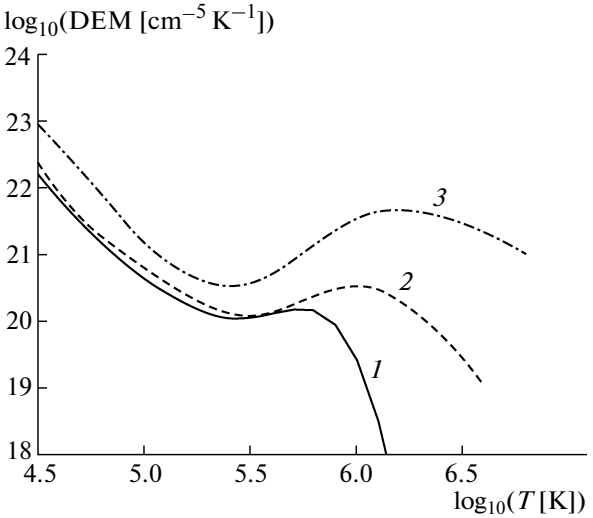

Fig. 17. Typical DEM distributions for the (*1*) CH, (*2*) QR, and (*3*) AR from the CHIANTI database.

excited levels of the given ion and the atomic constants for the corresponding transitions.

To determine the electron temperature T_e from the intensity ratio of the lines belonging to ions in the same charge state, lines with sufficiently different wavelengths are usually used. This is done to provide high sensitivity of the intensity ratio to the temperature, because, in this case, the dependence on T_e is mainly determined by the exponential factor $\exp(-\Delta E_{ik}/kT_e)$, where ΔE_{ik} is the difference between the energies of the ith and kth levels from which the corresponding lines are emitted. Moreover, in order to reliably determine the temperature, the ratio of the line intensities should also be insensitive to the electron density, which is usually verified by numerical calculations in the framework of the chosen collisional-radiative model.

The intensity ratios of the dielectronic satellites to the corresponding resonance line can be used to determine the temperature and ion composition of plasma. This is related to the presence of two mechanisms for the excitation of satellite lines: (i) dielectronic capture and (ii) direct excitation of an inner-shell electron of the ion with a smaller charge than the ion emitting the resonance line. The intensity ratio of the dielectronic satellite excited via the dielectronic mechanism to the resonance line is usually used to measure the electron temperature in ARs and flares, because the corresponding emission usually belongs to the X-ray band. From the intensity ratio of the collisionally excited dielectronic satellites to the resonance line, one can estimate the relative density of ions in different charge states. These ratios determine the plasma ionization temperature T_Z, i.e., they can be used to determine the deviation from equilibrium conditions in plasma. Measurements of the electron and ionization temperatures of plasma from the relative intensities of the resonance lines and their dielectronic satellites are widely used in studying astrophysical and laboratory plasmas. In particular, this approach is used for plasma diagnostics of solar flares from the spectra of He-like ions of Ca and Fe.

The electron density N_e can be determined from the intensity ratio of the lines emitted by the same ion. For example, in He-like ions, combinations of the intensity ratios of resonance, intercombination, and forbidden lines corresponding to K-transitions from the $n = 2$ levels are used for this purpose. This method is based on the fact that these ratios become sensitive to the density N_e when the rates of collisional transitions between excited states and other processes become comparable with the radiative transition probabilities of these levels.

In addition to the relative intensities, spectral line profiles are also used to measure the plasma ion temperature T_i. These measurements, however, are complicated by nonthermal motions of plasma. When measuring the kinetic temperatures of H and He ions, the main contribution to the line profiles is given by the Doppler broadening, which makes it possible to rather reliably measure the ion temperature from the widths of these lines. When measuring the ion temperature from the profiles of lines of other elements, it is usually assumed that the nonthermal component is the same for all ions under study (see, e.g., [76]). This approach can also be helpful to verify the often used assumption that $T_e = T_i$. For example, the authors of [76] applied this method to the plasma of CHs and found that the ion temperature T_i was substantially higher that the electron temperature T_e.

A more comprehensive description of the methods of coronal plasma diagnostics can be found, e.g., in [2].

4.3. Diagnostics of Hot Coronal Plasma according to the Data from the SPIRIT Experiment

During the *SPIRIT* experiment carried out onboard the *CORONAS-F* satellite from August 2001 to December 2005, the XUV channels of the *RES-C* spectroheliograph recorded several thousands of spectroheliograms in the spectral ranges of 176–207 and 280–330 Å. Together with EUV spectroheliograms, spectroheliograms recorded in the Mg XII 8.42-Å channel and XUV telescopic images were used to determine the position and time evolution of the region under study. Spectra of solar regions including various plasma structures (ARs, QRs, flares, above-limb structures, etc.) were analyzed, and a catalog of the spectral lines recorded by the XUV channels of the *RES-C* spectroheliograph was compiled [77].

Observations of the Sun in the Mg XII channel in the course of the *SPIRIT* experiment made it possible to reveal a new class of plasma structures with temper-

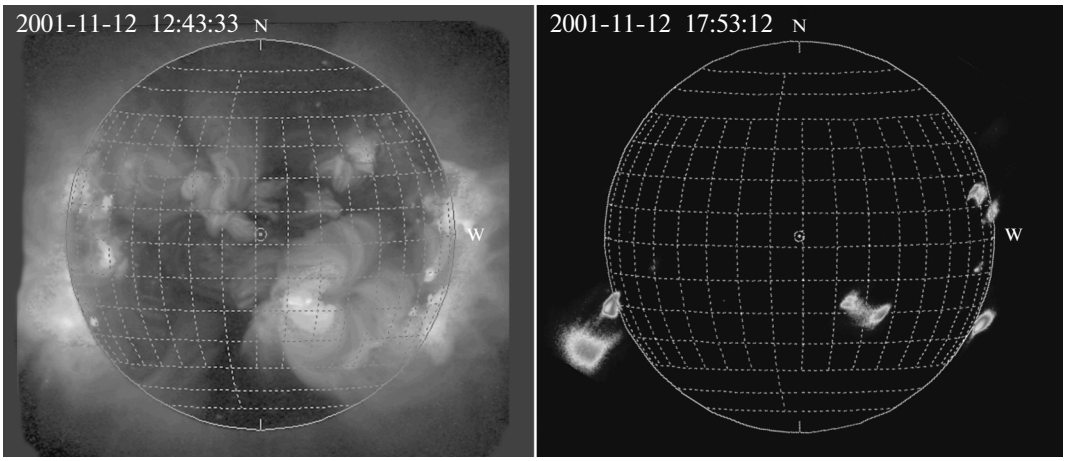

Fig. 18. Solar corona images recorded using the *SXT/Yohkoh* broadband telescope (on the left) and the Mg XII monochromatic channel of the *SPIRIT* complex (on the right) on November 12, 2001.

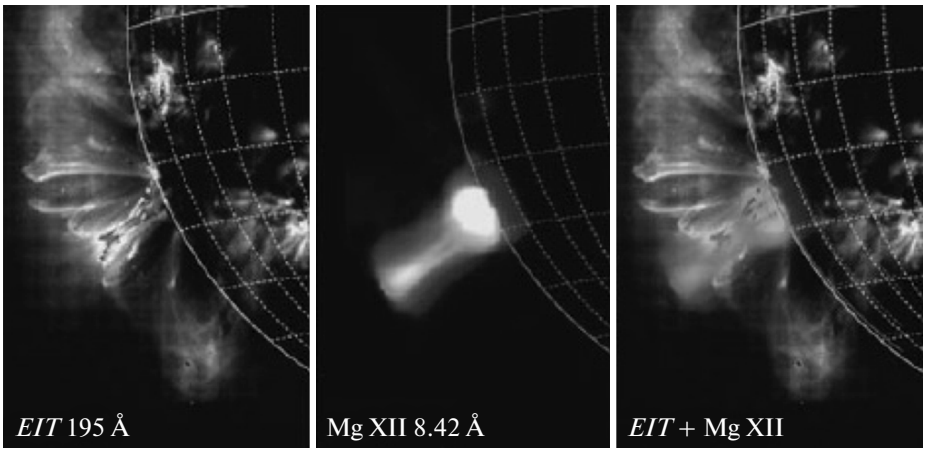

Fig. 19. Images of a coronal structure obtained using the hot Mg XII channel of *SPIRIT* and the cold 195-Å channel of *EIT/SOHO* on December 29, 2001.

atures of 4–20 MK and specific spatiotemporal behavior. This device represents an intermediate information channel between EUV telescopes recording moderate-temperature coronal plasma and *RHESSI*, which provides data on super-hot plasma. Regular observations in the Mg XII 8.42-Å line revealed new types of hot coronal structures with lifetimes from a few minutes to one day and characteristic dimensions from a few arc seconds to several tenths of the solar radius. In addition to the transient phenomena studied earlier at the *SXT/Yohkoh* satellite, a new class of dynamic structures with different shapes, dimensions, durations, and temporal characteristics, including long-lived (to several days) coronal structures located at heights of up to 300 000 km, was discovered. During a series of long-term (longer than 20 days) continuous observations performed with a high time resolution (0.6–1.7 min), high activity of such coronal structures, accompanied by the appearance of hot clouds, flaring phenomena, CMEs, etc., was also discovered. Figure 18 compares the images obtained on November 12, 2001, in the spectral channel of *SXT/Yohkoh* (sensitive in a wide temperature range of ~2.5–25 MK) and the *SPIRIT*/Mg XII channel (sensitive in the temperature range of ~5–15 MK).

Using spectral lines that are sensitive to temperatures in the range of 0.5–20 MK, but the emissivity functions $G_i(T)$ of which are not sensitive to the electron density under the coronal conditions, the DEM distributions were calculated for different solar structures by using the Bayesian iterative method (BIM) (see [75]). The emissivity functions were calculated using the CHIANTI atomic database [21]. The results of calculations with the use of the most reliably determined line intensities in the spectra of a number of

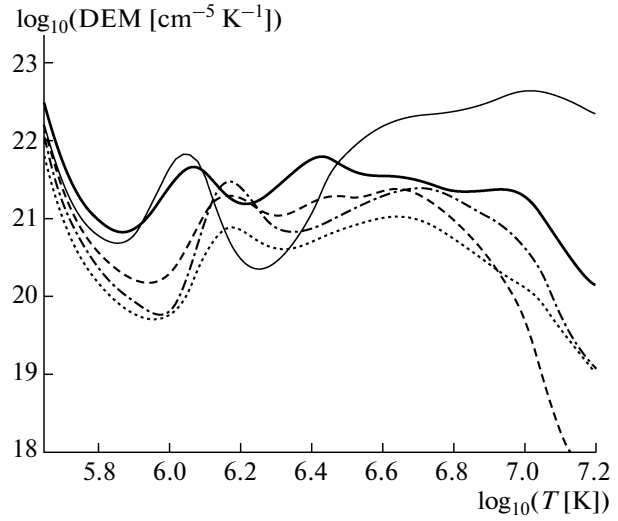

Fig. 20. DEM temperature distributions derived from the *SPIRIT* data for NOAA 9765 active region on the limb (heavy solid curve), a flare of class X3.4 (December 28, 2001) (light solid curve), and a coronal structure recorded in the Mg XII channel (December 28–29, 2001) for three heights above the limb: $h = 0.12R_\odot$ (dashed line), $h = 0.17R_\odot$ (dash-dotted line), and $h = 0.24R_\odot$ (dotted line).

active events were given in [74, 78]. An important result is the similarity between the DEM temperature distributions in ARs for a wide temperature range of up to 8 MK. It should also be noted that several radiation sources had a pronounced peak at a temperature of 10–12 MK.

Another important result of the diagnostics of hot plasma in active structures of the solar corona is the determination of the mechanism of SXR emission of coronal plasma structures by comparing the data obtained in the EUV and X-ray spectral bands [74]. The corresponding calculations were performed for the event observed on December 29, 2001 (see Fig. 19). Figure 19 shows images of this event recorded in the "hot" Mg XII channel of the *RES-C* spectroheliograph and the "cold" 195-Å channel of the *EIT* telescope installed at the *SOHO* satellite. In this figure, one can see a plasma structure stretched along the solar radius in the X-ray (hot) Mg XII image and a post-eruptive (cold) arcade of magnetic loops grouped in the perpendicular direction. Due to the convenient orientation of the *RES-C* instrument during the observation period (in the 280–330 Å XUV channel, this structure was oriented along the axis perpendicular to the dispersion direction), it was possible to study the DEM temperature distribution along the solar radius. Figure 20 shows these distributions for three distances from the solar limb, as well as for the AR at the limb. One can clearly see that the DEM temperature distribution (i.e., the distribution of the hot material) in the temperature range of 4–10 MK is inhomogeneous along the solar radius. For comparison, Fig. 20 also shows the DEM distribution for a flare of class X3.4 that occurred on December 28, 2001; it is seen that it has a pronounced temperature peak at 10–12 MK.

Figure 21 shows radial profiles of the intensities (normalized to their values on the solar limb) of individual EUV lines and the X-ray Mg XII line detected in the period in which there were no flares. An important result of such comparison is that the observed intensities of the EUV Ca XVIII line and X-ray Mg XII line, which are generated at nearly the same temperatures, behave in different ways: the intensity of the former decreases, whereas that of the latter increases. At the same time, the relative intensity of the Mg XII line calculated with the use of the distributions shown in Fig. 20 for the AR in the limb and three regions in the coronal structure recorded by the Mg XII channel (marked by crosses in Fig. 21) behaves similar to the observed intensity of the Ca XVIII line.

In [74], this result was explained as follows. Due to their relatively low excitation thresholds, the intensities of EUV lines are proportional to the emission measure formed by thermal (Maxwellian) electrons. The X-ray line of the Mg XII ion with a substantially higher excitation threshold is formed by high-energy electrons with energies on the order of 2 keV, the density of which in thermal plasma can comprise several percent of the total electron density. Therefore, the intensities of EUV lines do not depend on the presence of a small admixture of nonthermal (non-Maxwellian) electrons and are proportional to the thermal emission measure, while the intensity of the X-ray line is determined by the emissivity function, which can be much higher than its thermal value due to the presence of nonthermal electrons. Thus, it follows unambiguously from the observational data in the *RES-C* EUV channels that the emission mechanism of the hot plasma region in the solar limb (to the intensity of which the fluxes in Fig. 21 were normalized) is nonthermal (nonstationary). This conclusion agrees with the results obtained by analyzing the time profiles of the emission intensity in the Mg XII channel (see [74, 78] for details).

4.4. Diagnostics of Low-Density Plasma of the Extended Solar Corona

The coronal region located at distances from 1.5 to 10 solar radii (the extended corona) is of great importance in solar physics, because, at these heights, closed magnetic configurations transform into open ones, due to which conditions are created for the formation and acceleration of the solar wind, plasma heating, and acceleration of charged particle fluxes. In addition to observations in other spectral ranges (radio and visible ranges), EUV spectroscopy of the extended corona is an important tool for obtaining detailed information on coronal structures (such as CHs, streamers, and CMEs); the absolute abundances of

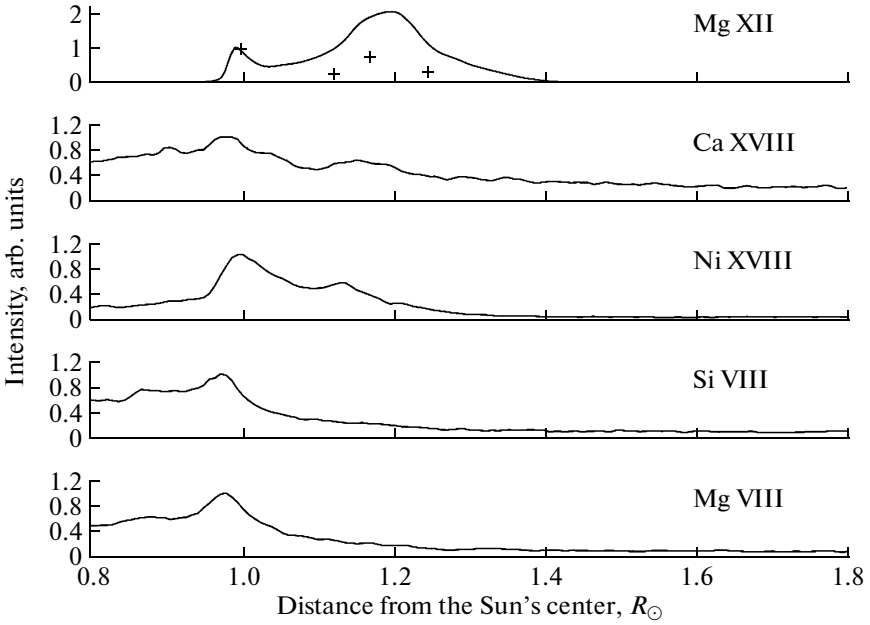

Fig. 21. Radial distributions of the intensities in EUV lines and in the Mg XII channel for the coronal structure occurred on December 29, 2001.

elements; and the velocity and density distributions of electrons, protons, and ions during the formation of the solar wind. Polarization measurements allow one, in principle, to determine the 3D configuration of the vector magnetic field. Below, we will consider the main methods of EUV spectroscopy of the extended corona on the basis of the review [79].

In the rocket experiments carried out in 1970s [80, 81], the H I Lyα resonance line emission was measured for the first time during the solar eclipse at distances of up to 1.5 solar radii. It was found that the corona radiates in this line due to the resonance scattering of the emission of the same spectral line generated in the chromosphere. In 1973–1974, the structure of the corona in polar CHs was studied and CMEs were observed for the first time on the *Skylab* orbital station [82] by using a white light coronagraph. These observations were continued (starting from 1995 up to the present) by using the *LASCO* coronagraph installed onboard the *SOHO* satellite. Simultaneously with observations in white light, thermal emission of the corona and bursts associated with shock waves generated in the course of CME development were studied in the radiowave range. Long-wavelength observations, including those performed during eclipses, allowed one to describe the general structure of the corona and manifestations of solar activity; however, they were insufficient to determine the physical conditions in the corona and mechanisms of the processes occurring in it, which became possible only due to the development of high-resolution spectroscopy.

Since the density of the extended corona decreases exponentially with height, the collisional plasma transforms into collisionless one. As a result, different ion components have different temperatures, different deviations from the Maxwellian EVDF, and different flow velocities. The element abundances and the ionization equilibrium vary substantially in different structures. Most of the extended corona emits resonance scattered radiation, which depends on the electron density in the first power, in contrast to radiation caused by collisions, which is proportional to the square of the electron density. Since the resonance lines of highly excited ions lie in the EUV band, the corresponding equipment and methods of EUV spectroscopy have been developed to study the extended corona. The most detailed studies were performed in 1995–2010 by using the *UltraViolet Coronagraph Spectrometer* (*UVCS*) installed onboard the *SOHO* space observatory [83].

The strongest emission line in all coronal structures is the Lyα resonance line of neutral atomic hydrogen with a wavelength of 1215.67 Å. The H Lβ (1025.72 Å), H Lγ (972.54 Å) and H Lδ (949.74 Å) lines are emitted in transitions from the higher levels. The *UVCS* operating range (500–1240 Å) also includes the spectral lines of ions of other elements with lower abundances, such as He I, C II–C III, N II, N III, N V, O I–O III, O V, O VI, Mg X, Si XII, S VI, Ca X, Fe XV, and Fe XVII.

Gabriel [81] considered five possible mechanisms for the generation of EUV line radiation of neutral hydrogen in the corona:

(i) electron-impact excitation,

(ii) photoexcitation by chromospheric hydrogen radiation,

(iii) Thomson scattering of chromospheric hydrogen radiation from free electrons of the coronal plasma,

(iv) Rayleigh scattering of chromospheric hydrogen radiation from ions, and

(v) scattering of chromospheric radiation from interplanetary dust.

Photoexcitation by hydrogen resonance radiation coming from the chromosphere makes the main contribution to the H Lyα line; however, in regions with an enhanced density (e.g., in CMEs), electron excitation can also contribute appreciably. The contribution from Thomson scattering of chromospheric hydrogen radiation is smaller by several orders of magnitude, and that from the rest components is even smaller. In the lower part of the corona, the largest contribution to other ion lines is made by collisional excitation. As the distance from the Sun increases, the contribution of collisional excitation to the line intensities decreases because of the decrease in the electron density, while the relative contribution of resonance scattering increases. The relative contributions of these mechanisms to the excitation depends on the kind of ions (the excitation temperature), the line oscillator strength, and the electron density; therefore, for different lines, the transition from collisional excitation to radiative one occurs at different distances from the Sun. The relation between collisional excitation and resonance scattering also depends on the plasma flow velocity. As was shown in Section 2.4, radial plasma motion leads to the Doppler shift of the absorption line with respect to the excitation line; as a result, the intensity of scattered radiation decreases (Doppler dimming). The effect of Doppler dimming, in addition to the flow velocity, also depends on the Doppler widths of the excitation and absorption lines.

The intensity of resonance scattered radiation is proportional to the product of the incident radiation flux by the density of a given kind of ions. Therefore, due to the high intensity of pumping radiation generated in the dense layers of the lower solar atmosphere, the lines of ions in low charge states, the excitation temperature of which is much lower than the coronal temperature and, accordingly, the density is much lower than the density of the main components, are observed experimentally in the corona.

The ionization equilibrium is an important factor affecting the intensity of lines emitted by the corona. At large distances, due to the low plasma density, the ionization equilibrium for many components can differ substantially from the state corresponding to the local electron temperature [84]. For plasma diagnostics, it is expedient to use pairs of lines corresponding to the same ion in order to eliminate uncertainties related to the ionization balance.

The coronal plasma is mainly optically thin; hence, the observed radiation is the sum of radiations emitted by all coronal structures along the line of sight. Therefore, when analyzing radiation from a certain structure, it is necessary to distinguish the contributions from this structure and its environment both behind and before it. For bright structures, such as streamers, the contribution from the surrounding background usually does not exceed 10%. The other conditions being the same, the largest contribution is provided by structures lying in the plane of the sky, i.e., being at the smallest distances from the solar surface, because their brightness is higher due to the higher plasma density.

The 3D structure of relatively stable structures of the coronal plasma, e.g., quiet equatorial streamers, can be determined using the tomographic reconstruction of plane-of-sky projections recorded during the rotation of the Sun around its axis (see, e.g., [85–87]). However, this method is applicable only to quasi-steady structures that do not change during the passage through the limb over several days [88]. An alternative method for determining the streamer size is to calculate its effective width along the line of sight (see [89]). If collisional excitation dominates, then, for the known values of the electron temperature and density over the streamer height, its effective width $L_\lambda(r)$ in a given spectral line as a function of the radius can be calculated by the formula

$$L_\lambda(r) = \frac{B_\lambda(r)}{G_\lambda(T(r))\left\langle N_e^2(r)\right\rangle},$$

where $B_\lambda(r)$ is the streamer brightness in this spectral line as a function on the radius, $G_\lambda(T(r))$ is the volume emission in the line λ per one ion at a temperature $T(r)$ (it can be calculated from atomic constants, e.g., by using the CHIANTI package [21]), and $\left\langle N_e^2(r)\right\rangle$ is the mean square of the electron density.

It follows from the aforesaid that the intensity of the EUV radiation of the extended corona is determined by the combination of many factors: the electron density and temperature, the abundance of a given element, the atomic constants of an ion (the line strength), the plasma flow velocity, the relation between the Doppler widths of the excitation and absorption lines, and the degree to which the condition of local coronal equilibrium is satisfied. It is not always possible to directly determine these parameters by the methods described in the previous sections because of the low radiation intensity. Therefore, the method of indirect diagnostics by simulating the intensity of emission lines in different spectral regions is more reliable. The parameters that can be determined experimentally are specified directly, while the other parameters are chosen so as to reduce the difference between the measured and calculated intensities to the values corresponding to the accuracy of measurements and calculations. Naturally, such simula-

tions require simplification of the problem by prescribing the profiles of the distributions of the unknown parameters over the height and width of the structure. An example of such a procedure is the determination of the parameters of the streamer plasma by simulating its emission in the visible and EUV spectral ranges and fitting the calculated intensities to the observational data [89].

4.5. Diagnostics of the Quiet Corona and Coronal Holes

The main method of identification of different types of coronal structures—ARs, QRs, and CHs—consists in measuring their relative brightnesses (with respect to the average brightness of the solar disk) in the SXR and EUV bands. According to data obtained using the *EIT* telescope, ARs with brightnesses exceeding the average brightness (with allowance for the dispersion of the signal) occupy a small fraction of the visible corona surface, from 8–10% in the solar minimum to 15–17% in the solar maximum (see Fig. 3). Most of the corona surface (85–66%) is occupied by vast QRs, the brightness of which corresponds to the average level of the corona surface), and 6–18% of the surface is occupied by CHs with brightnesses below the average level. The relative brightnesses of coronal structures and their dimensions depend substantially on the spectral range. For example, in the 195-Å channel of the *EIT* telescope, the ratio of the average AR brightness to the QR brightness is 2.5 in the minimum and 3.5 in the maximum of solar activity and the ratio between the CH and QR brightnesses is 0.5–0.6. The CH dimensions decrease with decreasing characteristic temperature of a spectral line. It should be noted that methods of plasma diagnostics based on measurements of the ratios between the spectral line intensities (see Section 4) are difficult to apply to CHs, because, in view of the low intensities of spectral lines, an appreciable contribution can be made by the scattered radiation of the neighboring brighter coronal structures. This contribution, however, can be excluded by correcting (deconvolving) the instrumental function of the device. It was demonstrated in [90] by recovering the images recorded using the *STEREO/EUVI* telescope in the solar minimum that, in CHs, scattered radiation can comprise up to 70% of the total signal level.

The plasma temperature and density in QRs were determined using the data obtained with the help of the *SUMER* spectrometer in the solar minimum (November 1996) at distances of $(1.03–1.5)R_\odot$ from the west limb [91]. The O VI, Ne VIII, Mg X, Si XI, Si XII, and Fe X–XII lines with excitation temperatures from 0.3 to 2 MK were used. Comparison of the line intensities calculated as functions of the temperature with their measured values showed that, at these distances from the Sun, plasma was nearly isothermal with a temperature of $T = 1.3 \pm 0.5$ MK. The electron density determined from the intensity ratio of the Si VIII lines varied from 1.8×10^8 cm^{-3} at a distance of $1.03R_\odot$ to 1.6×10^7 cm^{-3} at $1.3R_\odot$. It was noted in [91] that the intensities of the lines of Fe ions decreased with distance faster than those of the lines of lighter ions (Mg and Si), which was explained by the gravitational settling effect.

The temperature of the plasma of polar CHs was determined from the intensity ratio of the pairs of lines of Mg IX ions with wavelengths of 706 and 750 Å by using the data from the *SUMER* spectrometer [92]. The measurements were performed in the solar minimum in March, May, and November 1997 at distances of $(1.03–1.6)R_\odot$ above the north limb. Particular attention was paid to regions of the brighter polar plumes and interplume regions. It was found that the temperature in the plumes varied from 0.8 MK at the minimum distance to 0.33 MK at the maximum distance from the Sun, while in the interplume regions, it varied from 0.75 to 0.88 MK. The electron density determined from the intensity ratio of a pair of Si VIII lines varied from 10^8 to 10^7 cm^{-3} at $1.3R_\odot$ (in the plumes, the density was 1.5–2 times higher). It was found from the Doppler line broadening that the ion kinetic temperature substantially exceeded the electron temperature and varied from 4 to 10 MK. It was supposed that this effect could be related to plasma heating by ion-cyclotron oscillations. Later, taking into account more exact atomic data, the plasma temperature in the interplume region was increased to 1–1.5 MK and the nonthermal broadening was attributed to turbulent plasma motions with velocities of 20–50 km/s [93].

4.6. Spectroscopic Studies of Eruptive Phenomena

Various eruptive phenomena related to the outflow of dense low-temperature plasma from the lower layers of the atmosphere are observed in the solar corona. Plasma condensations with a temperature of $(6–8) \times 10^3$ K are often observed in the corona as filaments on the disk or prominences above the limb. They consist of the chromospheric substance and are usually situated at heights from 10^4 to 10^5 km. Their average density is $10^{11}–10^{12}$ cm^{-3}, which is two to three orders of magnitude higher than the density of the surrounding corona. The lifetime of these coronal structures is from several days to several solar rotations, and their stability is provided by the balance among the gravitation force, the gas-dynamic pressure, and the interaction between their magnetic self-field (from several units to a few hundred gauss) and the coronal magnetic field. When this balance is violated, the material of the prominence can be ejected by the magnetic forces to the external corona (the CME) or it can fall on the Sun's surface. According to the generally accepted terminology, CMEs are identified by the

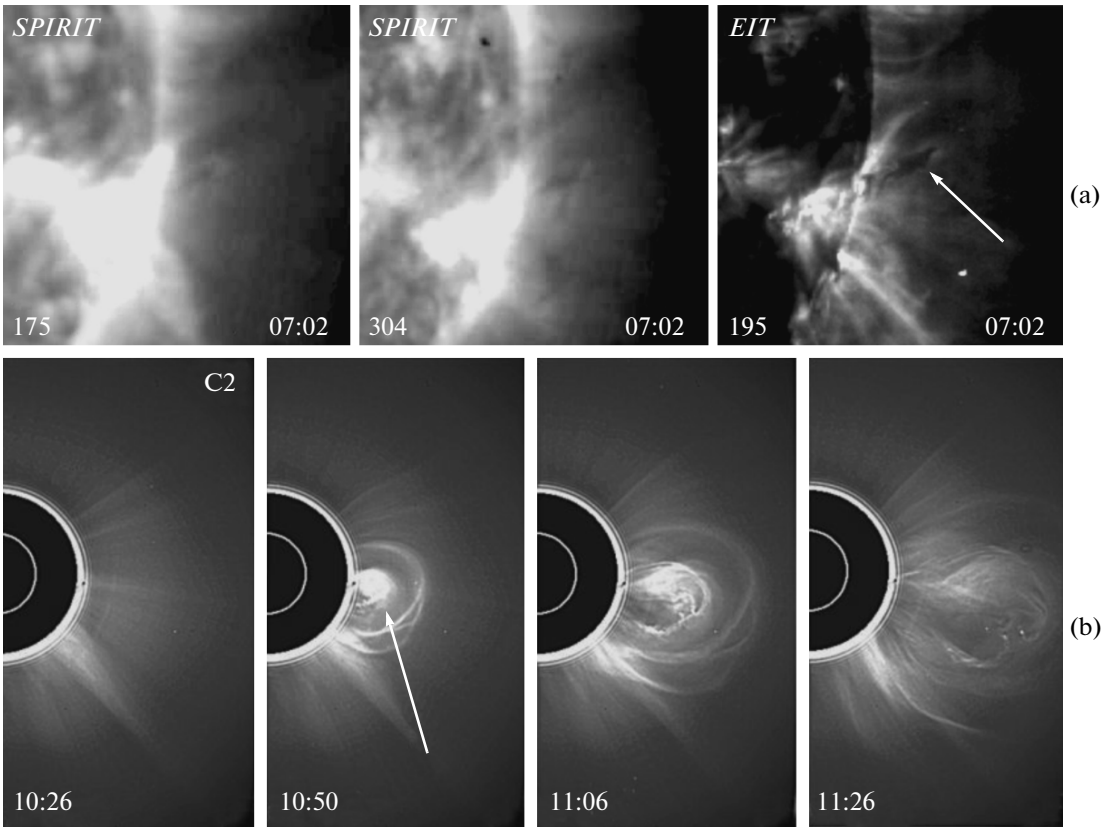

Fig. 22. Filament eruption (December 2, 2003) [100]: (a) initial eruption stage (a filament in the form of a dark structure (indicated by the arrow) against the corona background in the 175- and 304-Å lines (*SPIRIT*) and 195-Å line (*EIT*)) and (b) development of the CME observed using the *SOHO/LASCO C2* coronagraph in the visible range (the arrow indicates the CME core).

appearance of a bright structure with an angular size of several tens of degrees that propagates from the Sun in the field of view of a visible-light coronagraph over distances of larger than two solar radii from the limb. Other types of smaller scale nonstationary eruptive phenomena—spicules, surges, sprays, etc.—are usually related to the return of the material back to the Sun and do not lead to the formation of CMEs; however, they also contribute to the formation of the coronal medium in which CMEs develop and the solar wind forms. The physics of filaments, prominences, and other eruptive phenomena is considered in detail in monograph [94] and reviews [95, 96].

CMEs are the most powerful large-scale manifestations of solar activity. They are related to the reconstruction of the magnetic field in the large region of the solar atmosphere; therefore, they are an important object of spectroscopic studies. Under steady-state conditions, due to absorption of corona radiation in the relatively cold and dense filaments, they are observed in the EUV band as dark formations on the disk. The prominences are seen above the limb in their self-radiation, which forms in the transition region between the cold body of the prominence and the hot corona. CMEs develop as a result of magnetic reconnection in ARs and often occur simultaneously with flares, which are observed in the X-ray and EUV bands. The energy released during magnetic reconnection transforms into the radiation energy of the flare, the kinetic energy of the ejection, and the energy of accelerated charged particles. As a rule, CMEs have the so-called three-part structure consisting of the frontal structure formed by the shock wave, the dark gap, and the core formed from the initial filament. The velocity of the frontal structure in the corona region from the initial position of the prominence to $(3–5)R_\odot$ increases to 200–2000 km/s, whereas the velocity of the core is usually two times lower. During CMEs, regions with a depressed brightness (dimmings) form on the disk due to the escape of a fraction of the matter and post-eruption magnetic arcades with lifetimes from several hours to one day develop. Several models of the development of flares and CMEs have been elaborated to date [97–99]; however, none of them is universal, because it does not describe the entire scope of the observed phenomena.

Spectroscopic diagnostics of eruptive phenomena allows one to obtain information on the density, mass, and temperature of the material in the original filaments, prominences, and elements of the CME struc-

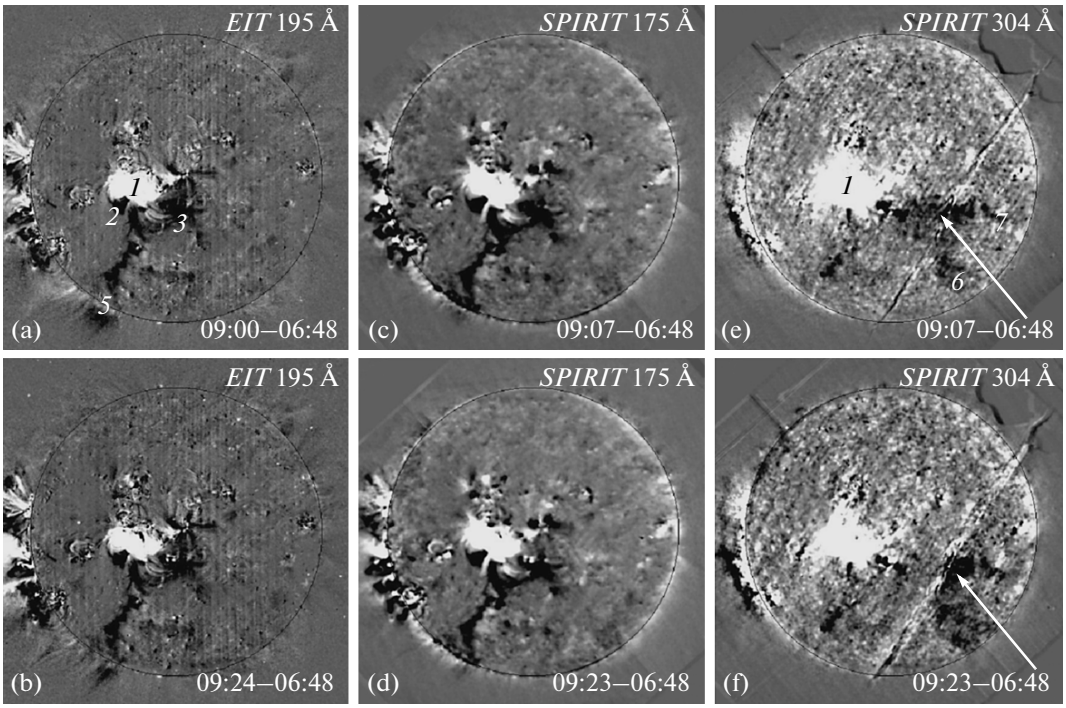

Fig. 23. Propagation of the plasma cloud (shown by the arrow) after the eruption of the filament (November 18, 2003) recorded in the 175-Å (on top) and 304-Å (on bottom) channels of the *SPIRIT* telescope [105].

ture. For this purpose, observations in one or several regions of the EUV band are performed simultaneously with observations in the visible and radio bands. Since CME develops and propagates relatively fast (on the average, the process of acceleration lasts from several tens of minutes to several hours), such observations should be performed simultaneously in different spectral ranges with a sufficient time resolution.

In [100], the filament eruption occurred on December 2, 2003, was observed in the Hα line in the ranges of 175 and 304 Å (*SPIRIT*) and 195 Å (*EIT*). As a result of eruption, a CME core formed from the filament material. The core first appeared in the UV band over the limb in the form of a dark structure against the background of the brighter corona. Later, it took the form of a bright structure in the CME image recorded by the *LASCO C2* coronagraph (Fig. 22). Photometric analysis of the absorption phenomena accompanying the eruption of filaments and prominences allows one to estimate the balance of the masses involved in the CME. In the coronal spectral lines (e.g., in the 175- and 195-Å bands), the darkening in the gaseous cloud against the background of the brighter surrounding corona is related to the following mechanisms: ionization of hydrogen and helium in the gaseous filament and the decrease in the brightness of this coronal region due to the absence of hot plasma generating coronal radiation in the given volume [101, 102]. Both ionization and resonance scattering contribute to the 304-Å line; however, the contribution of the latter manifests itself only in a narrow temperature range in which He II ions dominate and at plasma radial velocities as low as $v < 100$ km/s. At higher velocities, resonance scattering becomes inefficient because of the divergence of the Doppler contours of highlighting radiation and absorption by helium ions in the moving gas.

Estimates of the filament mass from absorption in coronal lines [100] yielded a value of 4×10^{15} g, which agrees well with the CME core mass of $(4–5) \times 10^{15}$ g estimated from the image recorded by the *SOHO/LASCO* visible-light coronagraph and confirms the origin of the CME core from the material of the erupted filament. According to the *LASCO* data, the total CME mass estimated from Thomson scattering of the visible radiation of the solar disk from electrons of the ejection plasma is 9×10^{15} g. This value is close to the upper limit of the CME mass, which, according to the statistics [103], lies in the range from 10^{13} to 10^{16} g.

In the event described in [104, 105], a cold plasma cloud formed from a part of the filament crossed almost the entire solar disk with a velocity of about 200 km/s, which, however, did not lead to CME formation (Fig. 23). Analysis showed that the origin of this phenomenon was the collision of the moving filament with a magnetic vortex, due to which the filament divided into two parts. After the interaction with

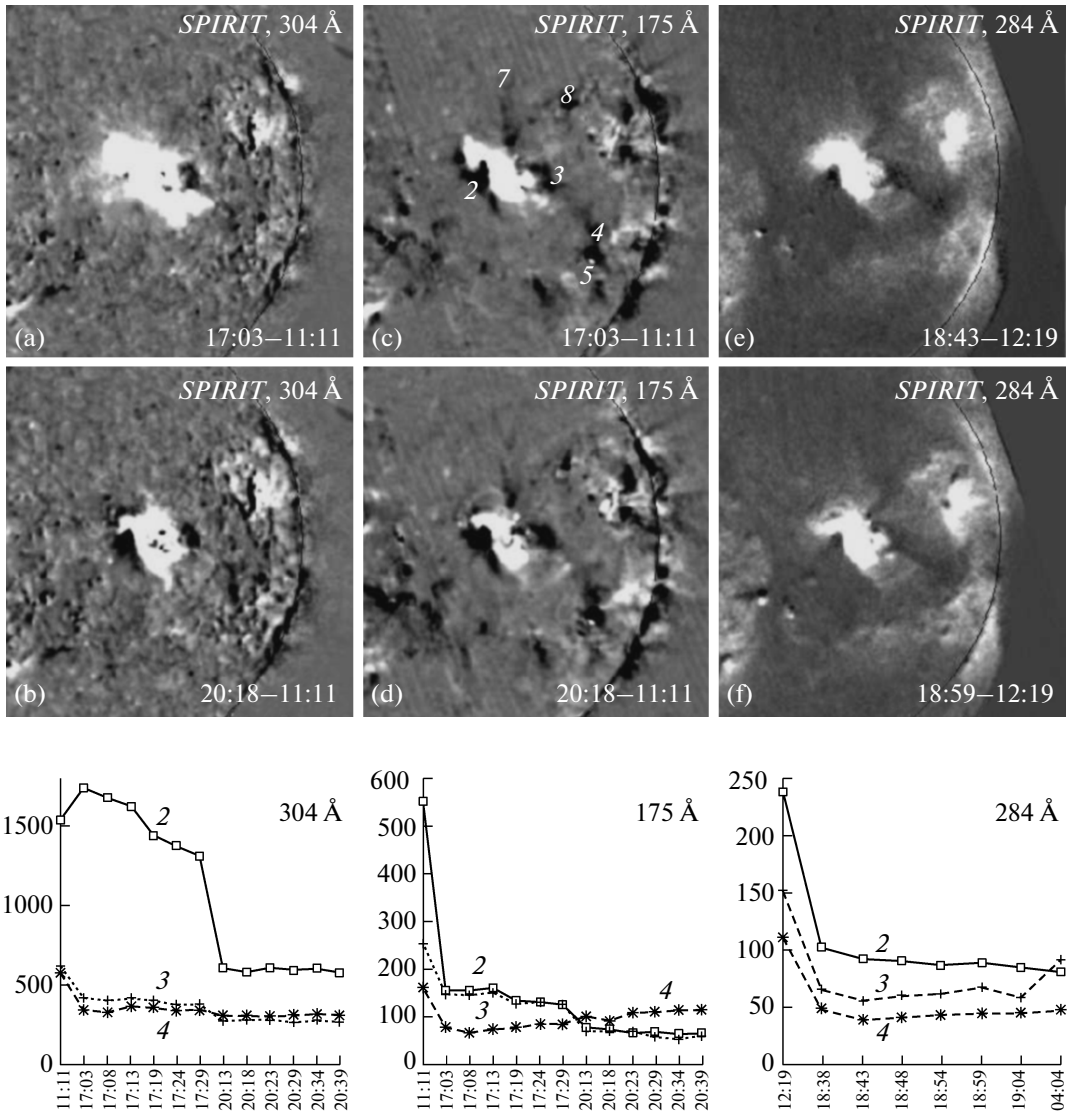

Fig. 24. (a–f) Dimmings observed using the *SPIRIT* telescope after the eruption occurred on November 4, 2001, and time evolution of the brightness in dimmings *2–4* (indicated in frame (c)) [110].

the vortex, the larger part transformed into the horizontally propagating cloud, whereas the smaller part formed a spheromac-type bunch of magnetized plasma (a magnetic cloud), which accelerated in the radial direction; detached from the Sun; and reached the Earth's magnetosphere with a velocity of 800–900 km/s, where it caused one of the strongest geomagnetic storms occurred during the 23th solar cycle.

Dimmings (or transient CHs) are regions with a depressed radiation intensity that form during CMEs in the vicinity of the eruption center and can cover a considerable part of the solar disk [106–108]. The localization and structure of the dimmings adjacent to the eruption center usually coincide in lines corresponding to different temperatures. This allows one to interpret them as a result of the complete or partial opening of the coronal magnetic fields, which leads to the escape of matter and the corresponding decrease in the radiation intensity. The outflow of matter from dimmings located near the eruption center was proven directly in [109], where the Doppler shifts of several EUV lines were measured.

Regular observations of the Sun by means of *SPIRIT* telescopes gave important information on the powerful eruptive events occurred in 2001–2005 [38]. An advantage of *SPIRIT* telescopes against other instruments (in particular, the *SOHO/EIT* telescope) was the possibility of simultaneously recording images of the entire solar disk in two spectral ranges: the 175-Å range, containing Fe IX–Fe XI coronal lines ($T \sim 0.9$–1.3 MK), and the 304-Å range, in which the He II line of the transition region ($T \sim 0.02$–0.08 MK) dominates. Comparison of time variations in the brightness of the structures observed in different spec-

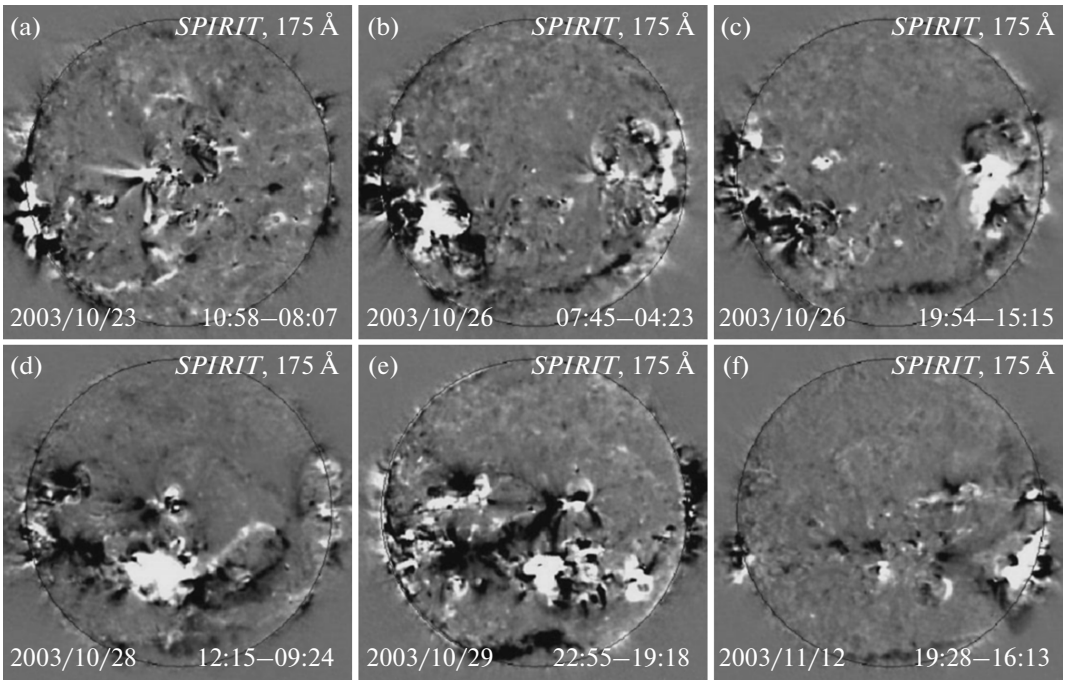

Fig. 25. Structure of dimmings observed in the 175-Å channel of the *SPIRIT* telescope in the events occurred from October 23 to November 2, 2003 [112].

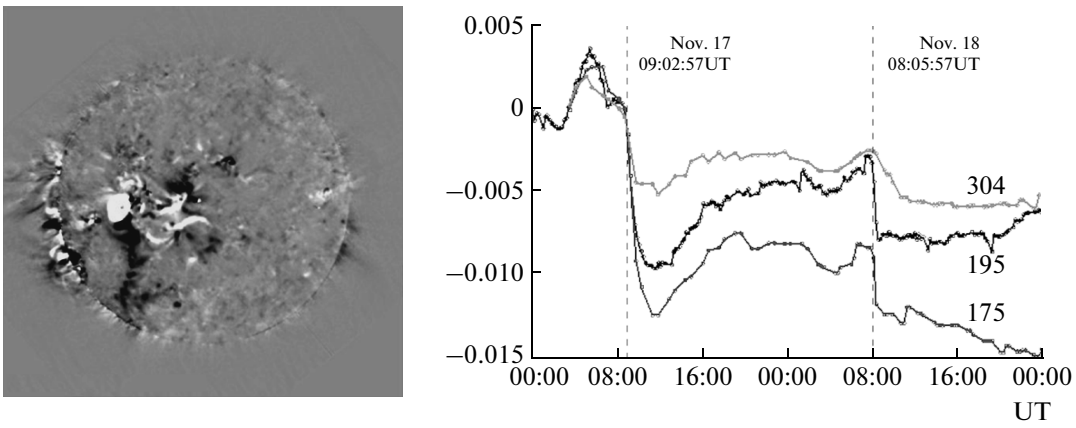

Fig. 26. Dimming formed as a result of CME occurred on November 17, 2003 at 09:02:57 UT and observed in the 175-Å channel of the SPIRIT telescope (on the left) and time evolution of the intensities integrated over the entire dimming region in the 175- and 304-Å channels of the *SPIRIT* telescope and the 195-Å channel of the *SOHO/EIT* telescope [113] (in fractions of the total intensity of the Sun).

tral ranges allowed one to study the propagation dynamics of perturbations in active processes, such as flares and CMEs. The other important problems were to establish global interrelations among activity centers and search for eruption precursors in order to forecast active phenomena and their geoefficiency.

In [110], the structure of dimmings formed in the eruptive event observed in the T1 (284 Å) and T2 (175 and 304 Å) channels of the *SPIRIT* telescope on November 4, 2001, was analyzed in detail. As a result of eruption, long-lived brightness depressions (dimmings) were observed in all EUV channels of *SPIRIT* (Fig. 24). These depressions were revealed using difference images obtained by subtracting an image obtained before the beginning of the event from a series of current images with allowance for Sun's rotation. In the bottom of Fig. 24, the time evolution of the integral intensity in the dimming regions corresponding to the formed CME (regions *2–4*) is shown. According to these data, the formation of dimmings

during the eruption develops from top to bottom, i.e., from the corona (the 175- and 284-Å lines) into the transition region (the He II 304-Å line), the dimming depth in the transition region being less than that in the corona.

Significant CMEs (including halo-type ones) occurred during the period of extremely high solar activity in October–November 2003. They were observed using the *SOHO/LASCO* white-light coronagraphs and the *SOHO/EIT* and *SPIRIT* EUV telescopes in the 175- and 304-Å channels [111]. Figure 25 shows the structure of dimmings observed in the 175-Å channel after the eruptive events occurred from October 23 to November 2, 2003. The large-scale character of the dimmings formed in the events of this series indicate that the formation of CMEs is a global process in which a considerable part of the solar atmosphere is involved.

The photometric analysis of the time evolution of the integral intensities of large-scale dimmings appeared during the formation of two CMEs on November 17 and 18, 2003, was performed in [112] (Fig. 26). It turned out that individual dimmings (even those appearing at large distances from the eruption center (the flare)) formed almost simultaneously. This indicates that there is a global interrelation among the corresponding magnetic structures, probably, via the so-called transequatorial magnetic loops, which are sometimes observed in the X-ray range and also manifest themselves as type-II bursts in the meter wavelength range [113, 114]. The interrelation among these structures, which leads to the correlation of brightness variations in remote dimmings, disappears after the magnetic field reconfiguration during the flare and CME formation; accordingly, the intensity correlation also disappears.

Photometric estimates of the total radiation intensity within large-scale dimmings shows that, in the peak of the dimming, the decrease in the intensity in coronal spectral lines can reach a significant value—from a fraction of percent to several percent of the total intensity of solar radiation in a given spectral range. This indicates that a considerable part of the solar corona is involved in the process of large-scale eruption and confirms the global character of this phenomenon of solar activity.

5. CONCLUSIONS

The results obtained in recent years by using spectroscopic methods of diagnostics as applied to such a complicated physical object as the solar corona demonstrate their high efficiency for both the better understanding of the processes occurring on the Sun and obtaining important information required to forecast space weather. The further development of these methods is based on an increase in the number of the simultaneously operating spectral channels; improvement of the spatial, temporal, and spectral resolutions; increased accuracy of observational data and their enhanced processing; and refinement of calculations of atomic characteristics and theoretical models describing the processes of plasma radiation in the wide range of conditions typical of the solar corona. The instruments for spectroscopic studies of the corona that are presently under development will allow one to study earlier inaccessible dynamic phenomena occurring on small spatial and temporal scales and reveal local and global interrelations of the processes at different levels of the solar atmosphere, thereby opening new ways of solving fundamental and applied problems of solar physics.

ACKNOWLEDGMENTS

We thank A.S. Shikanov for initiating this work and continuous support. This work was supported in part by the Russian Foundation for Basic Research (project no. 14-02-00945a) and eHEROES grant no. 284461 of the Seventh Frame Program of the European Commission. The *TEREK*, *SPIRIT*, and *TESIS* experiments were carried out at the Laboratory of X-ray Astronomy of the Sun, Lebedev Physical Institute, Russian Academy of Sciences, in the framework of the *CORONAS* program.

REFERENCES

1. M. J. Aschwanden, *Physics of the Solar Corona: An Introduction with Problems and Solutions* (Praxis, Chichester, 2005).
2. K. J. H. Phillips, U. Feldman, and E. Landi, *Ultraviolet and X-ray Spectroscopy of the Solar Atmosphere* (Cambridge Univ. Press, Cambridge, 2008).
3. L. Golub and J. M. Pasachoff, *The Solar Corona* (Cambridge Univ. Press, Cambridge, 2010).
4. J. M. Fontenla, E. H. Avrett, and R. Loeser, Astrophys. J. **355**, 700 (1990).
5. A. H. Gabriel, Philos. Trans. R. Soc. London **281**, 339 (1976).
6. J. E. Vernazza, E. H. Avrett, and R. Loeser, Astrophys. J. Suppl. **45**, 635 (1981).
7. Y.-M. Wang, J. B. Biersteker, N. R. Sheeley, Jr., S. Koutchmy, J. Mouette, amd M. Druckmuller, Astrophys. J. **660**, 882 (2007).
8. *Space Weather—Physics and Effects*, Ed. by I. A. Bothmer and I. A. Daglis (Praxis, Chichester, 2007).
9. G. A. Gary, Solar Phys. **203**, 71 (2001).
10. A. H. Gabriel, W. R. S. Garton, L. Goldberg, T. J. L. Jones, C. Jordan, F. J. Morgan, R. W. Nicholls, W. J. Parkinson, H. J. B. Paxton, E. M. Reeves, C. B. Shenton, R. J. Speer, and R. Wilson, Astrophys. J. **169**, 595 (1971).
11. G. L. Withbroe, J. L. Kohl, H. Weiser, and R. H. Munro, Space Sci. Rev. **33**, 17 (1982).
12. G. Noci, J. L. Kohl, and G. L. Withbroe, Astrophys. J. **315**, 706 (1987).

13. J. L. Kohl, G. Noci, S. R. Cranmer, and J. C. Raymond, Astron. Astrophys. Rev. **13**, 31 (2006).
14. S. R. Habbal, H. Morgan, J. Johnson, M. B. Arndt, A. Daw, S. Jaeggli, J. Kuhn, ad D. Mickey, Astrophys. J. **663**, 598 (2007).
15. N. Grevesse and A. J. Sauval, Space Sci. Rev. **85**, 161 (1998).
16. U. Feldman, Phys. Scr. **46**, 202 (1992).
17. U. Feldman and K. G. Widing, Space Sci. Rev. **107**, 665 (2003).
18. H. Peter, Astron. Astrophys. **335**, 691 (1998).
19. Y.-K. Ko, J. C. Raymond, T. H. Zurbuchen, P. Riley, J. M. Raines, and L. Strachan, Astrophys. J. **646**, 1275 (2006).
20. S. R. Habbal, M. Druckmuller, H. Morgan, A. Ding, J. Johnson, H. Druckmüllerová, A. Daw, M. B. Arndt, M. Dietzel, and J. Saken, Astrophys. J. **734**, 120 (2011).
21. K. P. Dere, E. Landi, H. E. Mason, B. C. Monsignori Fossi, and P. R. Young, Astron. Astrophys. Suppl. Ser. **125**, 149 (1997).
22. http://hesperia.gsfc.nasa.gov/ssw/packages/spex/doc/ospex_explanation.htm
23. R. K. Smith, N. S. Brickhouse, D. A. Liedahl, and J. C. Raymond, Astrophys. J. **556**, L91 (2001).
24. http://hea-www.harvard.edu/PINTofALE/
25. http://goes.gsfc.nasa.gov/text/goes.databook.html
26. S. Gburek, J. Sylwester, M. Kowaliński, M. Siarkowski, B. Sylwester, W. Trzebinski, S. V. Kuzin, A. A. Pertsov, Yu. D. Kotov, F. Farnik, F. Reale, and K. J. H. Phillips, Solar Phys. **283**, 631 (2013).
27. T. N. Woods, F. G. Eparvier, S. M. Bailey, P. C. Chamberlin, J. Lean, G. J. Rottman, S. C. Solomon, W. K. Tobiska, and D. L. Woodraska, J. Geophys. Res. A **110**, A01312 (2005).
28. M. Dominique, J.-F. Hochedez, W. Schmutz, I. E. Dammasch, A. I. Shapiro, M. Kretzschmar, A. N. Zhukov, D. Gillotay, Y. Stockman, and A. Ben-Mussa, Solar Phys. **286**, 21 (2013).
29. T. N. Woods, F. G. Eparvier, R. Hock, T. N. Woods, F. G. Eparvier, R. Hock, A. R. Jones, D. Woodraska, D. Judge, L. Didkovsky, J. Lean, J. Mariska, H. Warren, D. McMullin, P. Chamberlin, G. Berthiaume, S. Bailey, T. Fuller-Rowell, J. Sojka, W. K. Tobiska, and R. Viereck, Solar Phys. **275**, 115 (2012).
30. I. A. Zhitnik, Itogi Nauki Tekh., Astron. **9**, 7 (1974).
31. I. A. Zhitnik, I. P. Tindo, and A. M. Urnov, Tr. Fiz. Inst. im. P.N. Lebedeva, Akad. Nauk SSSR **195**, 3 (1989).
32. L. W. Acton, M. L. Finch, C. W. Gilbreth, J. L. Culhane, R. D. Bentley, J. A. Bowles, P. Guttridge, A. H. Gabriel, J. G. Firth, and R. W. Hayes, Solar Phys. **65**, 53 (1980).
33. Z. Kordylevski, Ya. Sil'vester, B. Sil'vester, M. Syarkovski, S. Plotsenyak, A. Kempa, M. Kovalinski, V. Tshebinski, and F. Farnik, in *Astrophysics and Space Science Library Series*, Vol. 400: *The Coronas-F Space Mission. Key Results for Solar Terrestrial Physics*, Ed. by V. D. Kuznetsov (Springer, Berlin, 2014), p. 149.
34. J. L. Culhane, E. Hiei, G. A. Doschek, A. M. Cruise, Y. Ogawara, Y. Uchida, R. D. Bentley, C. M. Brown, J. Lang, T. Watanabe, J. A. Bowles, R. D. Deslattes, U. Feldman, A. Fludra, P. Guttridge, A. Henins, J. Lapington, J. Magraw, J. T. Mariska, J. Payne, K. J. H. Phillips, P. Sheather, K. Slater, K. Tanaka, E. Towndrow, M. W. Trow, and A. Yamaguchi, Solar Phys. **136**, 89 (1991).
35. Z. Kordylevski, Ya. Sil'vester, B. Sil'vester, A. Kempa, M. Kovalinski, and V. Tshebinski, in *Astrophysics and Space Science Library Series*, Vol. 400: *The Coronas-F Space Mission. Key Results for Solar Terrestrial Physics*, Ed. by V. D. Kuznetsov (Springer, Berlin, 2014), p. 157.
36. I. L. Beigman, Itogi Nauki Tekh., Astron. **9**, 51 (1974).
37. I. A. Zhitnik, A. P. Ignatiev, V. V. Korneev, V. V. Krutov, S. V. Kuzin, A. V. Mitrofanov, S. Oparin, A. Pertsov, V. A. Slemzin, I. P. Tindo, M. Pakhomov, N. N. Salashchenko, and O. Timofeev, Proc. SPIE **3406**, 1 (1998).
38. I. A. Zhitnik, S. V. Kuzin, S. A. Bogachev, O. I. Bugaenko, Yu. S. Ivanov, A. P. Ignat'ev, V. V. Krutov, A. V. Mitrofanov, S. N. Oparin, A. A. Pertsov, V. A. Slemzin, N. K. Sukhodrev, I. I. Sobel'man, A. M. Urnov, and S. V. Shestov, in *Astrophysics and Space Science Library Series*, Vol. 400: *The Coronas-F Space Mission. Key Results for Solar Terrestrial Physics*, Ed. by V. D. Kuznetsov (Springer, Berlin, 2014), p. 129.
39. A. Reva, S. Kuzin, S. Bogachev, and S. Shestov, ASP Conf. Proc. **456**, 139 (2012).
40. G. S. Vaiana, L. van Speybroeck, M. V. Zombeck, A. S. Krieger, J. K. Silk, and A. Timothy, Space Sci. Instrum. **3**, 19 (1977).
41. J. H. Underwood, J. E. Milligan, A. C. Deloach, and R. B. Hoover, Appl. Opt. **16**, 858 (1977).
42. S. Tsuneta, L. Acton, M. Bruner, J. Lemen, W. Brown, R. Caravalho, R. Catura, S. Freeland, B. Jurcevich, M. Morrison, Y. Ogawara, T. Hirayama, and J. Owens, Solar Phys. **136**, 37 (1991).
43. L. Golub, E. Deluca, G. Austin, J. Bookbinder, D. Caldwell, P. Cheimets, J. Cirtain, M. Cosmo, P. Reid, A. Sette, M. Weber, T. Sakao, R. Kano, K. Shibasaki, H. Hara, S. Tsuneta, K. Kumagai, T. Tamura, M. Shimojo, J. McCracken, J. Carpenter, H. Haight, R. Siler, E. Wright, J. Tucker, H. Rutledge, M. Barbera, G. Peres, and S. Varisco, Solar Phys. **243**, 63 (2007).
44. R. P. Lin, B. R. Dennis, G. J. Hurford, D. M. Smith, A. Zehnder, P. R. Harvey, D. W. Curtis, D. Pankow, P. Turin, M. Bester, A. Csillaghy, M. Lewis, N. Madden, H. F. van Beek, M. Appleby, T. Raudorf, J. McTiernan, R. Ramaty, E. Schmahl, R. Schwartz, S. Krucker, R. Abiad, T. Quinn, P. Berg, M. Hashii, R. Sterling, R. Jackson, R. Pratt, R. D. Campbell, D. Malone, D. Landis, C. P. Barrington-Leigh, S. Slassi-Sennou, C. Cork, D. Clark, D. Amato, L. Orwig, R. Boyle, I. S. Banks, K. Shirey, A. K. Tolbert, D. Zarro, F. Snow, K. Thomsen, R. Henneck, A. McHedlishvili, P. Ming, M. Fivian, J. Jordan, R. Wanner, J. Crubb, J. Preble, M. Matranga, A. Benz, H. Hudson, R. C. Canfield, G. D. Holman, C. Crannell, T. Kosugi, A. G. Emslie, N. Vilmer, J. C. Brown,

C. Johns-Krull, M. Aschwanden, T. Metcalf, and A. Conway, Solar Phys. **210**, 3 (2002).

45. G. J. Hurford, E. J. Schmahl, R. A. Schwartz, A. J. Conway, M. J. Aschwanden, A. Csillaghy, B. R. Dennis, C. Johns-Krull, S. Krucker, R. P. Lin, J. McTiernan, T. R. Metcalf, J. Sato, and D. M. Smith, Solar Phys. **210**, 61 (2002).
46. I. A. Zhitnik, A. P. Ignat'ev, V. V. Korneev, V. V. Krutov, and V. M. Lomkova, Tr. Fiz. Inst. im. P.N. Lebedeva, Akad. Nauk SSSR **195**, 19 (1989).
47. I. I. Sobel'man, I. A. Zhitnik, A. P. Ignat'ev, V. V. Korneev, V. Yu. Klepikov, V. V. Krutov, S. V. Kuzin, A. V. Mitrofanov, S. N. Oparin, A. A. Pertsov, N. N. Salashchenko, V. A. Slemzin, A. I. Stepanov, I. P. Tindo, E. A. Avetisyan, V. M. Lomkova, V. F. Sukhanov, and Yu. N. Forin, Astron. Lett. **22**, 539 (1996).
48. J.-P. Delaboudinière, G. E. Artzner, J. Brunaud, A. H. Gabriel, J. F. Hochedez, F. Millier, X. Y. Song, B. Au, K. P. Dere, R. A. Howard, R. Kreplin, D. J. Michels, J. D. Moses, J. M. Defise, C. Jamar, P. Rochus, J. P. Chauvineau, J. P. Marioge, R. C. Catura, J. R. Lemen, L. Shing, R. A. Stern, J. B. Gurman, W. M. Neupert, A. Maucherat, F. Clette, P. Cugnon, and E. L. van Dessel, Solar Phys. **162**, 291 (1995).
49. B. N. Handy, L. W. Acton, C. C. Kankelborg, C. J. Wolfson, D. J. Akin, M. E. Bruner, R. Caravalho, R. C. Catura, R. Chevalier, D. W. Duncan, C. G. Edwards, C. N. Feinstein, S. L. Freeland, F. M. Friedlaender, C. H. Hoffmann, N. E. Hurlburt, B. K. Jurcevich, N. L. Katz, G. A. Kelly, J. R. Lemen, M. Levay, R. W. Lindgren, D. P. Mathur, S. B. Meyer, S. J. Morrison, M. D. Morrison, R. W. Nightingale, T. P. Pope, R. A. Rehse, C. J. Schrijver, R. A. Shine, L. Shing, K. T. Strong, T. D. Tarbell, A. M. Title, D. D. Torgerson, L. Golub, J. A. Bookbinder, D. Caldwell, P. N. Cheimets, W. N. Davis, E. E. Deluca, R. A. McMullen, H. P. Warren, D. Amato, R. Fisher, H. Maldonado, and C. Parkinson, Solar Phys. **187**, 229 (1999).
50. V. A. Slemzin, S. V. Kuzin, I. A. Zhitnik, J. P. Delaboudinière, F. Auchère, A. N. Zhukov, R. Linden, O. I. Bugaenko, A. P. Ignat'ev, A. V. Mitrofanov, A. A. Pertsov, S. N. Oparin, A. I. Stepanov, and A. N. Afanas'ev, Solar System Res. **39**, 489 (2005).
51. R. A. Howard, J. D. Moses, A. Vourlidas, J. S. Newmark, D. G. Socker, S. P. Plunkett, C. M. Korendyke, J. W. Cook, A. Hurley, J. M. Davila, W. T. Thompson, O. C. St. Cyr, E. Mentzell, K. Mehalick, J. R. Lemen, J. P. Wuelser, D. W. Duncan, T. D. Tarbell, C. J. Wolfson, A. Moore, R. A. Harrison, N. R. Waltham, J. Lang, C. J. Davis, C. J. Eyles, H. Mapson-Menard, G. M. Simnett, J. P. Halain, J. M. Defise, E. Mazy, P. Rochus, R. Mercier, M. F. Ravet, F. Delmotte, F. Auchere, J. P. Delaboudinière, V. Bothmer, W. Deutsch, D. Wang, N. Rich, S. Cooper, V. Stephens, G. Maahs, R. Baugh, D. McMullin, and T. Carter, Space Sci. Rev. **136**, 67 (2008).
52. S. V. Kuzin, S. A. Bogachev, I. A. Zhitnik, S. V. Shestov, V. A. Slemzin, A. V. Mitrofanov, N. K. Sukhodrev, A. A. Pertsov, A. P. Ignat'ev, O. I. Bugaenko, Yu. S. Ivanov, A. A. Reva, M. S. Zykov, A. S. Ul'yanov, S. N. Oparin, A. L. Goncharov, T. A. Shergina, A. M. Urnov, V. A. Solov'ev, and S. G. Popova, Bull. Russ. Acad. Sci. Phys. **74**, 33 (2010).
53. D. B. Seaton, D. Berghmans, B. Nicula, J.-P. Halain, A. De Groof, T. Thibert, D. S. Bloomfield, C. L. Raftery, P. T. Gallagher, F. Auchère, J.-M. Defise, E. D'Huys, J.-H. Lecat, E. Mazy, P. Rochus, L. Rossi, U. Schühle, V. Slemzin, M. S. Yalim, and J. Zender, Solar Phys. **286**, 43 (2013).
54. J. R. Lemen, A. M. Title, D. J. Akin, P. F. Boerner, C. Chou, J. F. Drake, D. W. Duncan, C. G. Edwards, F. M. Friedlaender, G. F. Heyman, N. E. Hurlburt, N. L. Katz, G. D. Kushner, M. Levay, R. W. Lindgren, D. P. Mathur, E. L. McFeaters, S. Mitchell, R. A. Rehse, C. J. Schrijver, L. A. Springer, R. A. Stern, T. D. Tarbell, J.-P. Wuelser, C. J. Wolfson, C. Yanari, J. A. Bookbinder, P. N. Cheimets, D. Caldwell, E. E. Deluca, R. Gates, L. Golub, S. Park, W. A. Podgorski, R. I. Bush, P. H. Scherrer, M. A. Gummin, P. Smith, G. Auker, P. Jerram, P. Pool, R. Soufli, D. L. Windt, S. Beardsley, M. Clapp, J. Lang, and N. Waltham, Solar Phys. **275**, 17 (2012).
55. A. V. Vinogradov, I. A. Brytov, and A. Ya. Grudskii, *Mirror X-ray Optics* (Mashinostroenie, Leningrad, 1989) [in Russian].
56. A. G. Michette, *Optical Systems for Soft X Rays* (Plenum, New York, 1986).
57. A. V. Mitrofanov, F. A. Pudonin, N. Starodubzev, and I. A. Zhitnik, Proc. SPIE **3406**, 35 (1998).
58. A. V. Mitrofanov and S. Yu. Zuev, Bull. Russ. Acad. Sci. Phys. **68**, 631 (2004).
59. S. A. Bogachev, S. V. Kuzin, V. A. Slemzin, and A. M. Urnov, in *Plasma Heliogeophysics*, Ed. by L. M. Zelenyi and I. S. Veselovskii (Fizmatlit, Moscow, 2008), Vol. 1, p. 140 [in Russian].
60. J. W. Brosius, R. J. Thomas, J. M. Davila, and E. Landi, Astrophys. J. **543**, 1016 (2000).
61. R. A. Harrison, E. C. Sawyer, M. K. Carter, A. M. Cruise, R. M. Cutler, A. Fludra, R. W. Hayes, B. J. Kent, J. Lang, D. J. Parker, J. Payne, C. D. Pike, S. C. Peskett, A. G. Richards, J. L. Gulhane, K. Norman, A. A. Breeveld, E. R. Breeveld, K. F. Al Janabi, A. J. McCalden, J. H. Parkinson, D. G. Self, P. D. Thomas, A. I. Poland, R. J. Thomas, W. T. Thompson, O. Kjeldseth-Moe, P. Brekke, J. Karud, P. Maltby, B. Aschenbach, H. Bräuninger, M. Kühne, J. Hollandt, O. H. W. Siegmund, M. C. E. Huber, A. H. Gabriel, H. E. Mason, and B. J. I. Bromage, Solar Phys. **162**, 233 (1995).
62. K. Wilhelm, W. Curdt, E. Marsch, U. Schühle, P. Lemaire, A. Gabriel, J.-C. Vial, M. Grewing, M. C. E. Huber, S. D. Jordan, A. I. Poland, R. J. Thomas, M. Kühne, J. G. Timothy, D. M. Hassler, and O. H. W. Siegmund, Solar Phys. **162**, 189 (1995).
63. W. Curdt, P. Brekke, U. Feldman, K. Wilhelm, B. N. Dwivedi, U. Schühle, and P. Lemaire, Astron. Astrophys. **375**, 591 (2001).
64. J. L. Culhane, L. K. Harra, A. M. James, K. Al-Janabi, L. J. Bradley, R. A. Chaudry, K. Rees, J. A. Tandy, P. Thomas, M. C. R. Whillock, B. Winter, G. A. Doschek, C. M. Korendyke, C. M. Brown, S. Myers, J. Mariska, J. Seely, J. Lang, B. J. Kent, B. M. Shaughnessy, P. R. Young, G. M. Simnett, C. M. Castelli,

S. Mahmoud, H. Mapson-Menard, B. J. Probyn, R. J. Thomas, J. Davila, K. Dere, D. Windt, J. Shea, R. Hagood, R. Moye, H. Hara, T. Watanabe, K. Matsuzaki, T. Kosugi, V. Hansteen, and Ø. Wikstol, Solar Phys. **243**, 19 (2007).

65. R. Tousey, J. D. F. Bartoe, J. D. Bohlin, G. E. Brueckner, J. D. Purcell, V. E. Scherrer, N. R. Sheeley, Jr., R. J. Schumacher, and M. E. Vanhoosier, Solar Phys. **33**, 265 (1973).
66. D. Müller, R. G. Marsden, O. C. St. Cyr, and H. R. Gilbert, Solar Phys. **285**, 25 (2013).
67. *Proceedings of the Workshop on the Interheliosond Project, Tarusa, 2011,* Ed. by V. D. Kuznetsov (IZMIRAN, Moscow, 2012).
68. B. De Pontieu, A. M. Title, J. R. Lemen, G. D. Kushner, D. J. Akin, B. Allard, T. Berger, P. Boerner, M. Cheung, C. Chou, J. F. Drake, D. W. Duncan, S. Freeland, G. F. Heyman, C. Hoffman, N. E. Hurlburt, R. W. Lindgren, D. Mathur, R. Rehse, D. Sabolish, R. Seguin, C. J. Schrijver, T. D. Tarbell, J.-P. Wülser, C. J. Wolfson, C. Yanari, J. Mudge, N. Nguyen-Phuc, R. Timmons, R. van Bezooijen, I. Weingrod, R. Brookner, G. Butcher, B. Dougherty, J. Eder, V. Knagenhjelm, S. Larsen, D. Mansir, L. Phan, P. Boyle, P. N. Cheimets, E. E. DeLuca, L. Golub, R. Gates, E. Hertz, S. McKillop, S. Park, T. Perry, W. A. Podgorski, K. Reeves, S. Saar, P. Testa, H. Tian, M. Weber, C. Dunn, S. Eccles, S. A. Jaeggli, C. C. Kankelborg, K. Mashburn, N. Pust, L. Springer, R. Carvalho, L. Kleint, J. Marmie, E. Mazmanian, T. M. D. Pereira, S. Sawyer, J. Strong, S. P. Worden, M. Carlsson, V. H. Hansteen, J. Leenaarts, M. Wiesmann, J. Aloise, K.-C. Chu, R. I. Bush, P. H. Scherrer, P. Brekke, J. Martinez-Sykora, B. W. Lites, S. W. McIntosh, H. Uitenbroek, T. J. Okamoto, M. A. Gummin, G. Auker, P. Jerram, P. Pool, and N. Waltham, Solar Phys. **289**, 2733 (2014).
69. Y. Katsukawa, T. Watanabe, H. Hara, K. Ichimoto, M. Kubo, K. Kusano, T. Sakao, T. Shimizu, Y. Suematsu, and S. Tsuneta, in *Proceedings of IAU Special Session 6. IAU XXVIII General Assembly, Beijing, 2012*, Paper E2.07.
70. S. R. Pottasch, Space Sci. Rev. **3**, 816 (1964).
71. J. T. Jefferies, F. Q. Orrall, and J. B. Zirker, Solar Phys. **22**, 307 (1972).
72. I. J. D. Craig and J. C. Brown, Astron. Astrophys. **49**, 239 (1976).
73. J. C. Brown, B. N. Dwivedi, Y. M. Almleaky, and P. A. Sweet, Astron. Astrophys. **249**, 277 (1991).
74. A. M. Urnov, S. V. Shestov, S. A. Bogachev, F. F. Goryaev, I. A. Zhitnik, and S. V. Kuzin, Astron. Lett. **33**, 396 (2007).
75. F. F. Goryaev, S. Parenti, A. M. Urnov, S. N. Oparin, J.-F. Hochedez, and F. Reale, Astron. Astrophys. **523**, A44 (2010).
76. C.-Y. Tu, E. Marsch, K. Wilhelm, and W. Curdt, Astrophys. J. **503**, 475 (1998).
77. S. V. Shestov, S. A. Bozhenkov, I. A. Zhitnik, S. V. Kuzin, A. M. Urnov, I. L. Beigman, F. F. Goryaev, and I. Yu. Tolstikhina, Astron. Lett. **34**, 33 (2008).
78. I. A. Zhitnik, S. V. Kuzin, A. M. Urnov, S. A. Bogachev, F. F. Goryaev, and S. V. Shestov, Solar System Res. **40**, 272 (2006).
79. J. L. Kohl, G. Noci, S. R. Granmer, and J. C. Raymond, Astron. Astrophys. Rev **13**, 31 (2006).
80. R. J. Speer, W. R. S. Garton, J. F. Morgan, R. W. Nicholls, L. Goldberg, W. H. Parkinson, E. M. Reeves, T. J. L. Jones, H. J. B. Paxton, D. B. Shenton, and R. Wilson, Nature **226**, 249 (1970).
81. A. H. Gabriel, Solar Phys. **21**, 392 (1971).
82. L. F. Belew and E. Stuhlinger, *Skylab* (Marshall Space Flight Center, Huntsville, AL, 1973).
83. J. L. Kohl, R. Esser, L. D. Gardner, S. Habbal, P. S. Daigneau, E. F. Dennis, G. U. Nystrom, A. Panasyuk, J. C. Raymond, P. L. Smith, L. Strachan, A. A. van Ballegooijen, G. Noci, S. Fineschi, M. Romoli, A. Ciaravella, A. Modigliani, M. C. E. Huber, E. Antonucci, C. Benna, S. Giordano, G. Tondello, P. Nicolosi, G. Naletto, C. Pernechele, D. Spadaro, G. Poletto, S. Livi, O. von der Lühe, J. Geiss, J. G. Timothy, G. Gloeckler, A. Allegra, G. Basile, R. Brusa, B. Wood, O. H. W. Siegmund, W. Fowler, R. Fisher, and M. Jhabvala, Solar Phys. **162**, 313 (1995).
84. G. L. Withbroe, J. L. Kohl, H. Weiser, and R. H. Munro, Space Sci. Rev. **33**, 17 (1982).
85. R. A. Frazin, Astrophys. J. **530**, 1026 (2000).
86. R. A. Frazin and P. Janzen, Astrophys. J. **570**, 408 (2002).
87. R. A. Frazin, S. R. Cranmer, and J. L. Kohl, Astrophys. J. **597**, 1145 (2003).
88. A. M. Vasquez, Zh. Huang, W. B. Manchester, and R. A. Frazin, Solar Phys. **274**, 259 (2011).
89. F. Goryaev, V. Slemzin, L. Vainshtein, and D. R. Williams, Astrophys. J. **781**, 100 (2014).
90. P. Shearer, R. A. Frazin, A. O. Hero, and A. C. Gilbert, Astrophys. J. Lett. **749** (2012).
91. U. Feldman, G. A. Doschek, U. Schühle, and K. Wilhelm, Astrophys. J. **518**, 500 (1999).
92. K. Wilhelm, E. Marsch, B. N. Dwivedi, D. M. Hassler, P. Lemaire, A. H. Gabriel, and M. C. E. Huber, Astrophys. J. **500**, 1023 (1998).
93. K. Wilhelm, Space Sci. Rev. **172**, 57 (2012).
94. B. P. Filippov, *Eruptive Processes on the Sun* (Fizmatlit, Moscow, 2007) [in Russian].
95. R. Schwenn, J. C. Raymond, D. Alexander, A. Ciaravella, N. Gopalswamy, R. Howard, H. Hudson, P. Kaufmann, A. Klassen, D. Maia, G. Munoz-Martinez, M. Pick, M. Reiner, N. Srivastava, D. Tripathi, A. Vourlidas, and Y.-M. Wang, J. Zhang, Space Sci. Rev. **123**, 127 (2006).
96. M. Pick, T. G. Forbes, G. Mann, H. V. Cane, J. Chen, A. Ciaravella, H. Cremades, R. A. Howard, H. S. Hudson, A. Klassen, K. L. Klein, M. A. Lee, J. A. Linker, D. Maia, Z. Mikic, J. C. Raymond, M. J. Reiner, G. M. Simnett, N. Srivastava, D. Tripathi, R. Vainio, A. Vourlidas, J. Zhang, T. H. Zurbuchen, N. R. Sheeley, and C. Marqué, Space Sci. Rev. **123**, 341 (2006).
97. J. Lin and T. G. Forbes, J. Geophys. Res. **105**, 2375 (2000).

98. E. R. Priest and T. Forbes, *Magnetic Reconnection: MHD Theory and Applications* (Cambridge Univ. Press, Cambridge, 2000).
99. T. G. Forbes, J. A. Linker, J. Chen, C. Cid, J. Kóta, M. A. Lee, G. Mann, Z. Mikić, M. S. Potgieter, J. M. Schmidt, G. L. Siscoe, R. Vainio, S. K.Antiochos, and P. Riley, Space Sci. Rev. **123**, 251 (2006).
100. S. Koutchmy, V. Slemzin, B. Filippov, J.-C. Noens, D. Romeuf, and L. Golub, Astron. Astrophys. **483**, 599 (2008).
101. P. Heinzel, U. Anzer, B. Schmieder, and P. Schwartz, in *Proceedings of the ISCS 2003 Symposium "Solar Variability as an Input to the Earth's Environment," Tatranska Lomnica, 2003*, Ed. by A. Wilson (ESA, Noordwijk, 2003), p. 447.
102. U. Anzer and P. Heinzel, Astrophys. J. **622**, 714 (2005).
103. N. Gopalswamy, J. Astrophys. Astron. **27**, 243 (2006).
104. V. V. Grechnev, I. M. Chertok, V. A. Slemzin, S. V. Kuzin, A. P. Ignat'ev, A. A. Pertsov, I. A. Zhitnik, J.-P. Delaboudinière, and F. Auchère, J. Geophys. Res. **110**, A09S07 (2005).
105. V. V. Grechnev, A. M. Uralov, I. M. Chertok, V. A. Slemzin, B. P. Filippov, Y. I. Egorov, V. G. Fainshtein, A. N. Afanasyev, N. P. Prestage, and M. Temmer, Solar Phys. **289**, 1279 (2014).
106. I. M. Chertok and V. V. Grechnev, Astron. Rep. **47**, 139 (2003).
107. I. M. Chertok and V. V. Grechnev, Astron. Rep. **47**, 934 (2003).
108. A. N. Zhukov and I. S. Veselovsky, Astrophys. J. **664**, L131 (2007).
109. L. K. Harra and A. C. Sterling, Astrophys. J. **561**, L215 (2001).
110. I. M. Chertok, V. A. Slemzin, S. V. Kuzin, V. V. Grechnev, O. I. Bugaenko, I. A. Zhitnik, A. P. Ignat'ev, and A. A. Pertsov, Astron. Rep. **48**, 407 (2004).
111. S. Kuzin, I. Chertok, V. Grechnev, V. Slemzin, O. Bugaenko, I. Zhitnik, A. Ignat'ev, and A. Pertsov, Adv. Space Res. **38**, 451 (2006).
112. V. Slemzin, S. Kuzin, and S. Bogachev, in *Proceedings of the SPM-11 Conference "The Dynamic Sun: Challenges for Theory and Observations," Leuven, 2005*, Paper P.166.1.
113. J. I. Khan and H. S. Hudson, Geophys. Rev. Lett. **27**, 1083 (2000).
114. S. Pohjolainen, N. Vilmer, J. I. Khan, and A. E. Hillaris, Astron. Astrophys. **434**, 329 (2005).

Translated by L. Mosina